A High-Order WENO Finite Difference Scheme for the Equations of Ideal Magnetohydrodynamics

Guang-Shan Jiang* and Cheng-chin Wu†

*Courant Institute, 251 Mercer Street, New York, New York 10012; †Department of Physics
and Astronomy, University of California, Los Angeles, California 90095
E-mail: gsj@cims.nyu.edu, wu@physics.ucla.edu

We present a high-order accurate weighted essentially non-oscillatory (WENO) finite difference scheme for solving the equations of ideal magnetohydrodynamics (MHD). This scheme is a direct extension of a WENO scheme, which has been successfully applied to hydrodynamic problems. The WENO scheme follows the same idea of an essentially non-oscillatory (ENO) scheme with an advantage of achieving higher-order accuracy with fewer computations. Both ENO and WENO can be easily applied to two and three spatial dimensions by evaluating the fluxes dimension-by-dimension. Details of the WENO scheme as well as the construction of a suitable eigen-system, which can properly decompose various families of MHD waves and handle the degenerate situations, are presented. Numerical results are shown to perform well for the one-dimensional Brio–Wu Riemann problems, the two-dimensional Kelvin–Helmholtz instability problems, and the two-dimensional Orszag–Tang MHD vortex system. They also demonstrate the importance of maintaining the divergence free condition for the magnetic field in achieving numerical stability. The tests also show the advantages of using the higher-order scheme. The new 5th-order WENO MHD code can attain an accuracy comparable with that of the second-order schemes with many fewer grid points. © 1999 Academic Press

Key Words: magnetohydrodynamics; essentially non-oscillatory scheme.

1. INTRODUCTION

In this paper, a high-order accurate weighted essentially non-oscillatory (WENO) finite difference scheme is presented for solving the ideal magnetohydrodynamics (MHD) equations

$$\rho_t = -\nabla \cdot (\rho \mathbf{v}), \tag{1.1}$$

561

$$(\rho\mathbf{v})_t = -\nabla \cdot \left[\rho\mathbf{v}\mathbf{v} + \overleftrightarrow{I}\left(p + \frac{1}{2}B^2 \right) - \mathbf{B}\mathbf{B} \right], \tag{1.2}$$

$$\mathbf{B}_t = \nabla \times (\mathbf{v} \times \mathbf{B}), \tag{1.3}$$

$$\varepsilon_t = -\nabla \cdot \left[\left(\frac{\gamma}{\gamma - 1}p + \frac{1}{2}\rho v^2 \right)\mathbf{v} - (\mathbf{v} \times \mathbf{B}) \times \mathbf{B} \right]. \tag{1.4}$$

Here ρ, p, $\mathbf{v}$, $\mathbf{B}$, and ε denote the mass density, the hydrodynamic pressure, the velocity field, the magnetic field, and the total energy, respectively. The ratio of the specific heats is given by γ and $\varepsilon = \frac{1}{2}\rho v^2 + \frac{1}{2}B^2 + p/(\gamma - 1)$. In addition to these equations, the magnetic field satisfies the divergence free condition, $\nabla \cdot \mathbf{B} = 0$.

The WENO schemes are based on the essentially non-oscillatory (ENO) schemes, which were first developed by Harten *et al.* [12] in the form of finite volume schemes and were later improved by Shu and Osher [27] into a more efficient and easy-to-implement finite difference form. The ENO schemes are generalizations of the total variation diminishing (TVD) schemes of Harten [11]. The TVD schemes typically degenerate to first-order accuracy at locations with smooth extrema while the ENO schemes maintain high-order accuracy there even in multi-spatial dimensions. Despite their high-order accuracy, ENO schemes are as capable as TVD schemes in suppressing spurious oscillations in the numerical solution.

The key idea of the ENO schemes is to use the smoothest stencil among several candidates to approximate the fluxes at the cell boundaries to high order and at the same time to avoid spurious oscillations near shocks and discontinuities. The WENO schemes go one step further by taking a weighted average of all candidates. The weights are adjusted by the local smoothness of the solution so that essentially zero weights are given to non-smooth stencils while optimal weights are prescribed in smooth regions. Around the discontinuities, WENO schemes behave similarly to ENO schemes, but in the smooth regions of the solution, WENO schemes act more like an upstream centered scheme. In principle, any rth order accurate ENO scheme can be "converted" to a $(2r - 1)$st order accurate WENO scheme.

The first version of WENO schemes was developed by Liu *et al.* [17] in finite volume formulation for one-dimensional conservation laws. Later, Jiang and Shu [14] presented a finite difference version of WENO schemes for multidimensional conservation laws and also optimized the accuracy of the scheme with a new weighting procedure. The finite difference WENO scheme, which has been extensively tested on multidimensional hydrodynamic problems [14, 35], is applied here for the MHD code.

As in many other modern shock capturing methods, our WENO scheme is based on the local characteristic decomposition of waves. The fluxes are first separated into each family of waves. Then they are split into positive and negative parts by either global or local Lax–Friedrichs flux splitting. Subsequently, the fluxes at the cell boundaries are constructed by the WENO approximation.

Because of the wave decomposition procedure, considerable work is required to evaluate the MHD eigensystem. There are seven waves in the MHD system. In addition to the entropy wave, which propagates with the fluid speed, v, there are three wave modes, which can propagate with two $v \pm c$ speeds, where c denotes the characteristic speed of the mode. According to the magnitude of the wave speeds, these three modes are called fast, intermediate (Alfvén), and slow waves. The fast and slow waves are compressive, while the intermediate wave is not. Depending on the direction and the magnitude of the magnetic field, these wave speeds may coincide. Thus the MHD equations form a non-strictly hyperbolic

system. In spite of this, a complete set of eigenvectors can be found and, with proper normalizations, they are well-defined [4, 22].

The jump relations of the MHD system are equally complicated. There are six entropy-satisfying shock jump relations. Two are fast and slow shocks. The other four transitions are called intermediate shocks. For a fast shock, there is a pair of converging fast waves into the shock. Similarly, there is a pair of slow waves converging into a slow shock. For one type of intermediate shock, one has a pair of converging intermediate waves. The other three types of intermediate shocks are over-compressive, which can have converging fast waves, or slow waves, or both, in addition to intermediate waves. There are limiting cases when one of the converging characteristics has the same speed as the shock. Thus compound waves, where a shock is attached by a rarefaction wave or a rarefaction wave is attached by a shock, can be formed, as was first observed by Brio and Wu [3, 4]. Besides the shock waves, there are other discontinuities in the MHD Rankine–Hugoniot relations. They include contact discontinuity, tangential discontinuity, and rotational discontinuity.

Since the MHD system is not genuinely nonlinear [3, 4], one may question the validity of using shock capturing schemes for its calculations. Indeed, in a series of numerical and analytical studies [33, 34, 15], it is shown that whenever a rotation of the magnetic field occurs, the evolution of the MHD system may depend on the dissipation mechanism, which according to the Navier–Stokes MHD equations, includes bulk and shear viscosities, resistivity, and heat conductivity. Thus two different shock capturing schemes with different numerical dissipation terms can produce two different solutions. Furthermore, a capturing scheme may not lead to convergent results as the sizes of the time step and the grid spacing are refined because the numerical dissipation terms may change in the process. The situation stems from the fact that the shock structure of intermediate shocks is generally not unique. Our new code, which is a shock capturing scheme, has the same drawback. We envision that one can correct the situation by selectively in the computation including the dissipative terms for resolving intermediate shock structures.

Another numerical issue in the MHD calculation concerns the condition of $\nabla \cdot \mathbf{B} = 0$. While this condition is formally ensured if it is satisfied by the initial data, the numerical truncation errors can lead to nonzero value. Since our code is of high-order accuracy in the smooth region, the errors in this condition should be small and should vanish in the limiting sense. However, across a discontinuity, the truncation error is of first order and the problem can be serious. This issue has been considered by many authors and several remedies have been tried [2, 36, 24, 20, 5, 9, 8]. We have experimented with a scheme that enforces the condition by a correction method [2, 36, 24]. First we solve for the potential ϕ for the Poisson equation, $\nabla^2 \phi + \nabla \cdot \mathbf{B} = 0$, with $\mathbf{B}$ the updated magnetic field obtained by the WENO scheme. Then we compute the corrected magnetic field as $\mathbf{B}^c = \mathbf{B} + \nabla \phi$, for which $\nabla \cdot \mathbf{B}^c = 0$.

In the last decade, several schemes, which share some common aspects with our scheme, have been developed for the MHD equations. In 1988, Brio and Wu [4] presented the first second-order upwind TVD scheme for one spatial dimension where they successfully constructed a Roe matrix [21] for the MHD equations in the case of $\gamma = 2$. Degeneracies of the eigen-system were treated by them with proper normalization to remove singularities that can occur. Later, the scheme was extended to multidimensional flow by Ryu *et al.* [23, 24] and by Tanaka [29]. Aslan [1] also followed the idea of the Roe scheme to construct a second-order upwind MHD scheme by a fluctuation approach. Another interesting upwind scheme was developed by Powell *et al.* [20] following

the same line of the Roe scheme [21]. They also proposed an eight-wave family eigen-system instead of the usual seven-wave family eigen-system. Their method will be employed in constructing our 8×8 eigen-system. Zachary *et al.* [36] applied an operator splitting technique and devised a high order Godunov type scheme. Recently, Dai and Woodward [7] proposed an approximate Riemann solver for obtaining numerical fluxes at cell interface. They have incorporated artificial viscosity to handle strong shocks. All the schemes mentioned above have been successfully applied to multidimensional MHD equations.

We have developed a set of 5th-order accurate semi-discrete WENO MHD codes in one, two, and three spatial dimensions. The application to higher spatial dimensions is achieved by computing the fluxes dimension-by-dimension. The 4th-order Runge–Kutta scheme of Shu [25] is used for the time evolution. The new MHD codes do well in calculating the solutions of one-dimensional MHD Riemann problems and the two-dimensional evolution of the Kelvin–Helmholtz instability in a magnetized system. They have also provided solutions for the Orszag–Tang turbulence model [18]. The numerical tests show that maintaining the divergence-free condition for the magnetic field is important in achieving numerical stability. They also show the advantages of using the higher-order scheme.

The outline of the paper is as follows: In Section 2, we define the WENO scheme and present the eigen-systems for the MHD equations. The numerical results are presented in Section 3. Some remarks are made in Section 4.

2. THE NUMERICAL METHOD

Since the formulation of the ENO scheme in the finite volume form by Harten *et al.* [12], there have been many improvements in the methodology. In this paper, a finite difference version of Shu and Osher [27], with its extension to the WENO idea by Jiang and Shu [14], is applied to the MHD code. The finite difference formulation, which is based on point values, has proved to be more computationally efficient than the finite volume scheme. The method can be generalized in a straightforward manner to multi-spatial dimensions. A detailed account of the construction, analysis, and application of ENO/WENO schemes is recently provided by Shu [26]. In this section, we define the scheme we use in the paper, including the choice of flux splitting and the characteristic decomposition.

We first describe the basic idea of the WENO scheme which involves the computation of the cell-interface values of an one-dimensional function from its cell averages at the neighboring cells. We then present the WENO scheme for conservation laws. In the last subsection, we describe the eigen-system for the MHD equations, including its left- and right-eigenvectors, which are required for wave projections.

2.1. *The Basic Idea of the WENO Approximation*

Let $h(x) : [0, 1] \rightarrow R$ be a piecewise smooth function. We discretize the interval $[0, 1]$ into uniform spaced subintervals with grid points $x_i = i \Delta x, 0 \leq i \leq N$ and $\Delta x = 1/N$. Define the *sliding average* of $h(x)$ over an interval Δx as

$$\bar{h}_\Delta(x) = \frac{1}{\Delta x} \int_{x-\frac{\Delta x}{2}}^{x+\frac{\Delta x}{2}} h(s) \, ds. \tag{2.1}$$
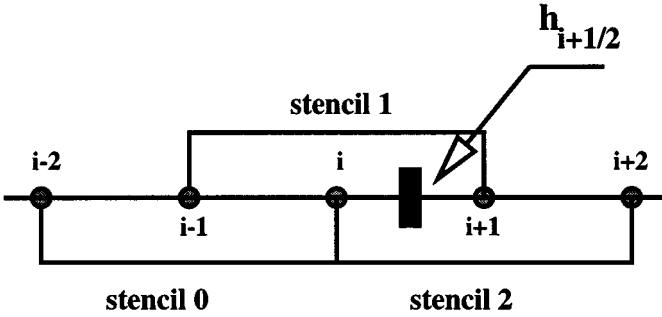
FIG. 1.   The three sub-stencils.

Suppose that $\bar{h}_k = \bar{h}_\Delta(x_k)$ is known for $k = i - 2, i - 1, i, i + 1$, and $i + 2$, the WENO approximation of $h(x_{i+1/2})$ $(x_{i+1/2} = x_i + \Delta x/2)$ possesses the following two properties:

(1) If $h(x)$ is smooth near $x_{i+1/2}$, the approximated value $h_{i+1/2}$ of $h(x_{i+1/2})$ satisfies

$$h_{i+\frac{1}{2}} = h\left(x_{i+\frac{1}{2}}\right) + O(\Delta x^5).$$

(2) If $h(x)$ is discontinuous near $x_{i+1/2}$, no Gibbs phenomena (i.e., spurious oscillations) occur.

The idea of the WENO scheme is to weight properly the three sub-stencils of the five-point stencil x_k, $i - 2 \le k \le i + 2$ (see Fig. 1). In each sub-stencil s $(s = 0, 1, 2)$ the 3rd-order accurate approximation $h_{i+1/2}^s$ to $h(x_{i+1/2})$ is obtained by the Taylor series expansion of $h(x)$ as

$$h_{i+\frac{1}{2}}^0 = \frac{1}{3}\bar{h}_{i-2} - \frac{7}{6}\bar{h}_{i-1} + \frac{11}{6}\bar{h}_i,$$

$$h_{i+\frac{1}{2}}^1 = -\frac{1}{6}\bar{h}_{i-1} + \frac{5}{6}\bar{h}_i + \frac{1}{3}\bar{h}_{i+1},$$

$$h_{i+\frac{1}{2}}^2 = \frac{1}{3}\bar{h}_i + \frac{5}{6}\bar{h}_{i+1} - \frac{1}{6}\bar{h}_{i+2}.$$

The WENO approximation of $h(x_{i+1/2})$ assumes the form

$$h_{i+\frac{1}{2}} = \omega_0 h_{i+\frac{1}{2}}^0 + \omega_1 h_{i+\frac{1}{2}}^1 + \omega_2 h_{i+\frac{1}{2}}^2, \tag{2.2}$$

where ω_0, ω_1, ω_2 are the positive weights[1] with $\omega_0 + \omega_1 + \omega_2 = 1$. Replacing ω_1 by $1 - \omega_0 - \omega_2$ and also using the three 3rd-order formulae in (2.2), we get

$$h_{i+\frac{1}{2}} = \frac{1}{12}(-\bar{h}_{i-1} + 7\bar{h}_i + 7\bar{h}_{i+1} - \bar{h}_{i+2}) + \frac{1}{3}\omega_0(\bar{h}_{i-2} - 3\bar{h}_{i-1} + 3\bar{h}_i - \bar{h}_{i+1})$$

$$+ \frac{1}{6}\left(\omega_2 - \frac{1}{2}\right)(\bar{h}_{i-1} - 3\bar{h}_i + 3\bar{h}_{i+1} - \bar{h}_{i+2}).$$

[1] Notice that the 5th approximation to $h(x_{i+1/2})$ based on the five-point stencil x_k, $i - 2 \le k \le i + 2$, is given by $\frac{1}{30}\bar{h}_{i-2} - \frac{13}{60}\bar{h}_{i-1} + \frac{47}{60}\bar{h}_i + \frac{9}{20}\bar{h}_{i+1} - \frac{1}{20}\bar{h}_{i+2}$ or equivalently $\frac{1}{12}(-\bar{h}_{i-1} + 7\bar{h}_i + 7\bar{h}_{i+1} - \bar{h}_{i+2}) - \frac{1}{30}(-\bar{h}_{i-2} + 4\bar{h}_{i-1} - 6\bar{h}_i + 4\bar{h}_{i+1} - \bar{h}_{i+2})$. If we choose $w_0 = 0.1$, $w_1 = 0.6$, $w_2 = 0.3$, (2.2) becomes identical to this. These constants are called optimal weights and are reflected in the numerators in the definitions of α_0, α_1, and α_2.

This can be rewritten in the form

$$h_{i+\frac{1}{2}} = \frac{1}{12}(-\bar{h}_{i-1} + 7\bar{h}_i + 7\bar{h}_{i+1} - \bar{h}_{i+2}) - \varphi_N\left(\Delta\bar{h}_{i-\frac{3}{2}}, \Delta\bar{h}_{i-\frac{1}{2}}, \Delta\bar{h}_{i+\frac{1}{2}}, \Delta\bar{h}_{i+\frac{3}{2}}\right), \quad (2.3)$$

where $\Delta\bar{h}_{k+\frac{1}{2}} = \bar{h}_{k+1} - \bar{h}_k$ for any integer k and

$$\varphi_N(a, b, c, d) = \frac{1}{3}\omega_0(a - 2b + c) + \frac{1}{6}\left(\omega_2 - \frac{1}{2}\right)(b - 2c + d).$$

Now, to complete the description of the WENO approximation, we need to prescribe the weights ω_0 and ω_2. They are chosen so that both properties (1) and (2) are attained. A detailed discussion of the selection is given in Jiang and Shu [14]. Using their choice, we define ω_0 and ω_2 by

$$\omega_0 = \frac{\alpha_0}{\alpha_0 + \alpha_1 + \alpha_2}, \qquad \omega_2 = \frac{\alpha_2}{\alpha_0 + \alpha_1 + \alpha_2}$$

$$\alpha_0 = \frac{1}{(\epsilon + IS_0)^2}, \qquad \alpha_1 = \frac{6}{(\epsilon + IS_1)^2}, \qquad \alpha_2 = \frac{3}{(\epsilon + IS_2)^2}$$

$$IS_0 = 13(a - b)^2 + 3(a - 3b)^2, \qquad IS_1 = 13(b - c)^2 + 3(b + c)^2,$$

$$IS_2 = 13(c - d)^2 + 3(3c - d)^2.$$

Here $\epsilon = 10^{-6}$ is used to prevent the denominators from becoming zero. According to Jiang and Shu [14], the result is not sensitive to ϵ as long as it is in the range of 10^{-5} to 10^{-7}. Notice that φ_N is a nonlinear function because ω_0, ω_2 are nonlinear functions of $a, b, c,$ and d.

Similarly, from values of $\bar{h}_k = \bar{h}(x_k)$ for $k = i - 1, i, i + 1, i + 2,$ and $i + 3$, the WENO approximation of $h(x_{i+1/2})$ is given by

$$h_{i+\frac{1}{2}} = \frac{1}{12}(-\bar{h}_{i-1} + 7\bar{h}_i + 7\bar{h}_{i+1} - \bar{h}_{i+2}) + \varphi_N\left(\Delta\bar{h}_{i+\frac{5}{2}}, \Delta\bar{h}_{i+\frac{3}{2}}, \Delta\bar{h}_{i+\frac{1}{2}}, \Delta\bar{h}_{i-\frac{1}{2}}\right). \quad (2.4)$$

2.2. The WENO Scheme for Conservation Laws

In this subsection, we describe a finite difference version of the ENO/WENO scheme. We start with the formulation for 1D, first for a scalar equation, and then for a system. Then we present the procedure for a system of conservation laws in 2D, whose extension to 3D is obvious.

For a 1D scalar equation

$$u_t = -f(u)_x, \quad (2.5)$$

the scheme uses a conservative approximation to the spatial derivatives,

$$\frac{du_i(t)}{dt} = -\frac{1}{\Delta x}\left(\hat{f}_{i+\frac{1}{2}} - \hat{f}_{i-\frac{1}{2}}\right) \quad (2.6)$$

where $u_i(t)$ is the numerical approximation to the point value $u(x_i, t)$ in a uniform grid and the numerical flux

$$\hat{f}_{i+\frac{1}{2}} = \hat{f}(u_{i-r}, \dots, u_{i+s})$$

is required to be a Lipschitz continuous function in all the arguments and also to be consistent with the physical flux, i.e., $\hat{f}(u, \ldots, u) = f(u)$.

For achieving numerical stability and for avoiding entropy violating solutions, upwinding and flux splitting approaches are used in constructing the flux. The flux is written as a sum of the positive and negative fluxes, $f^{\pm}(u)$,

$$f(u) = f^+(u) + f^-(u), \qquad (2.7)$$

where

$$\frac{df^+(u)}{du} \geq 0 \qquad (2.8)$$

$$\frac{df^-(u)}{du} \leq 0. \qquad (2.9)$$

Thus for the equation $u_t + f_x^+ = 0$, the wave propagates in the increasing x direction, while for $u_t + f_x^- = 0$, it goes the other way. There are several choices for defining the flux. A simple choice is given by the Lax–Friedrichs splitting, which produces very smooth fluxes,

$$f^{\pm}(u) = \frac{1}{2}(f(u) \pm \alpha u), \qquad (2.10)$$

where α is taken as $\max_u |f'(u)|$ over the relevant range of u. If the range is locally defined, it is called the local Lax–Friedrichs splitting; if the range is global, it is called the global Lax–Friedrichs splitting. For lower order schemes the quality of the solution is usually very sensitive to the choice of the spltting, and the Lax–Friedrichs flux is very diffusive. But this sensitivity is much less important for a higher-order method.

We then apply the WENO approximation procedure, as was given in Subsection 2.1 to $f^{\pm}(u)$ to obtain two numerical fluxes $\hat{f}^{\pm}_{i+1/2}$, and sum them up to obtain the numerical flux $\hat{f}_{i+1/2}$. The 5th-order WENO approximations, (2.3) and (2.4), give

$$\hat{f}^+_{i+\frac{1}{2}} = \frac{1}{12}(-f^+_{i-1} + 7f^+_i + 7f^+_{i+1} - f^+_{i+2}) - \varphi_N\left(\Delta f^+_{i-\frac{3}{2}}, \Delta f^+_{i-\frac{1}{2}}, \Delta f^+_{i+\frac{1}{2}}, \Delta f^+_{i+\frac{3}{2}}\right) \quad (2.11)$$

$$\hat{f}^-_{i+\frac{1}{2}} = \frac{1}{12}(-f^-_{i-1} + 7f^-_i + 7f^-_{i+1} - f^-_{i+2}) + \varphi_N\left(\Delta f^-_{i+\frac{5}{2}}, \Delta f^-_{i+\frac{3}{2}}, \Delta f^-_{i+\frac{1}{2}}, \Delta f^-_{i-\frac{1}{2}}\right), \quad (2.12)$$

where $\Delta f^+_{k+1/2} = f^+_{k+1} - f^+_k$ and similarly for the negative flux components. Note that the idea of upwinding is applied here: $\hat{f}^+_{i+1/2}$ is obtained from the five-point stencil for k from $i - 2$ to $i + 2$, and $\hat{f}^-_{i+1/2}$ is obtained from the five-point stencil for k from $i - 1$ to $i + 3$. Adding together $\hat{f}^+_{i+1/2}$ and $\hat{f}^-_{i+1/2}$ gives the numerical flux $\hat{f}_{i+1/2}$, which depends on six grid values at $i - 2, \ldots, i + 3$:

$$\hat{f}_{i+\frac{1}{2}} = \frac{1}{12}(-f_{i-1} + 7f_i + 7f_{i+1} - f_{i+2}) - \varphi_N\left(\Delta f^+_{i-\frac{3}{2}}, \Delta f^+_{i-\frac{1}{2}}, \Delta f^+_{i+\frac{1}{2}}, \Delta f^+_{i+\frac{3}{2}}\right)$$

$$+ \varphi_N\left(\Delta f^-_{i+\frac{5}{2}}, \Delta f^-_{i+\frac{3}{2}}, \Delta f^-_{i+\frac{1}{2}}, \Delta f^-_{i-\frac{1}{2}}\right). \qquad (2.13)$$

This completes the spatial discretization procedure for a scalar equation according to the 5th-order WENO scheme. The time evolution is provided by high-order accurate Runge–Kutta schemes, which are presented at the end of the section.

There are several ways to generalize the ENO/WENO schemes to systems of conservation laws. Our choice is to use characteristic decomposition, which is more robust, but more computationally intensive, than other simpler implementations. The finite difference version of the ENO/WENO scheme again solves the system of conservation laws

$$U_t = -F(U)_x, \tag{2.14}$$

in the conservative form

$$\frac{dU_i(t)}{dt} = -\frac{1}{\Delta x}\left(\hat{F}_{i+\frac{1}{2}} - \hat{F}_{i-\frac{1}{2}}\right), \tag{2.15}$$

where U and F are vectors of the m component: $U = (u_1, u_2, \ldots, u_m)^\top$, $F(U) = (f_1(U), f_2(U), \ldots, f_m(U))^\top$. Here we again assume the grid is uniform.

The characteristic decomposition procedure proceeds in the following way: Based on the values of U_i and U_{i+1}, a mean Jacobian $A_{i+1/2}$ is defined at the interface $x_{i+1/2}$. For the MHD code, we take $A_{i+1/2}$ to be the Jacobian $\partial F/\partial U$ of the system evaluated for some average state $U_{i+1/2}$, which is a function of U_i and U_{i+1}. Their exact definitions are given in Subsection 2.3. The eigenvalues of the matrix A correspond to the wave speeds of the system. As noted in the Introduction, although the eigenvalues in the MHD system can be degenerate, a complete set of eigenvectors can be found. Let us denote the right eigenvectors of A by R_s and, correspondingly, the left eigenvectors by L_s for $s = 1, \ldots, m$. The right eigenvector is a column vector and the left eigenvector is a row vector, both with m components. By proper normalization, $L_r \cdot R_s = \delta_{rs}$.

Given $R_{i+1/2}$ and $L_{i+1/2}$, the physical fluxes at $k = i - 2, \ldots, i + 3$ are projected into the right eigenvector space,

$$F_k = \sum_{s=1}^{m} F_k^s R_{i+\frac{1}{2}}^s \tag{2.16}$$

with $F_k^s = L_{i+1/2} \cdot F_k$. The physical meaning of this step is that the system is decomposed into a set of locally independent linear equations. Now we use the technique in the scalar case to find the numerical flux $\hat{F}_{i+1/2}^s$ at $i + \frac{1}{2}$ for each component. The Lax–Friedrichs flux splitting is used to separate the flux into positive and negative parts: $F_k^{s\pm} = (F_k^s \pm \alpha_s U_k^s)/2$. Here, $U_k^s = L_{i+1/2} \cdot U_k$, representing the characteristic variable and α^s is the maximum value of the sth eigenvalue of $A_{k+\frac{1}{2}}$, either over the entire range of k for the global flux splitting or over $(i - 2, \ldots, i + 3)$ for the local flux splitting. Thus, from (2.13), the WENO approximation gives

$$\hat{F}_{i+\frac{1}{2}}^s = \frac{1}{12}\left(-F_{i-1}^s + 7F_i^s + 7F_{i+1}^s - F_{i+2}^s\right) - \varphi_N\left(\Delta F_{i-\frac{3}{2}}^{s+}, \Delta F_{i-\frac{1}{2}}^{s+}, \Delta f_{i+\frac{1}{2}}^{s+}, \Delta F_{i+\frac{3}{2}}^{s+}\right)$$

$$+ \varphi_N\left(\Delta F_{i+\frac{5}{2}}^{s-}, \Delta F_{i+\frac{3}{2}}^{s-}, \Delta F_{i+\frac{1}{2}}^{s-}, \Delta F_{i-\frac{1}{2}}^{s-}\right).$$

From (2.16), we finally obtain the numerical flux as

$$\hat{F}_{i+\frac{1}{2}} = \frac{1}{12}(-F_{i-1} + 7F_i + 7F_{i+1} - F_{i+2})$$

$$+ \sum_{s=1}^{m}\left(-\varphi_N\left(\Delta F_{i-\frac{3}{2}}^{s+}, \Delta F_{i-\frac{1}{2}}^{s+}, \Delta F_{i+\frac{1}{2}}^{s+}, \Delta F_{i+\frac{3}{2},j}^{s+}\right)\right.$$

$$\left.+ \varphi_N\left(\Delta F_{i+\frac{5}{2}}^{s-}, \Delta F_{i+\frac{3}{2}}^{s-}, \Delta F_{i+\frac{1}{2}}^{s-}, \Delta F_{i-\frac{1}{2}}^{s-}\right)\right) R_{i+\frac{1}{2}}^s. \tag{2.17}$$

Since for 2D and 3D, the conservative approximation to the derivative can be obtained in a dimension-by-dimension fashion, the scheme can be applied to 2D and 3D in a simple manner. The following is the complete WENO scheme in 2-D. Let the uniform two-dimensional lattice grid points be $(x_i, y_j) = (i\Delta x, j\Delta y)$ with $0 \le i \le N_x, 0 \le i \le N_y$ and $\Delta x = 1/N_x$, $\Delta y = 1/N_y$. For a system of conservation laws

$$U_t = -F(U)_x - G(U)_y, \qquad 0 < x, y < 1, \tag{2.18}$$

where $U = (u_1, u_2, \ldots, u_m)^\top$, $F(U) = (f_1(U), f_2(U), \ldots, f_m(U))^\top$ and $G(U) = (g_1(U), g_2(U), \ldots, g_m(U))^\top$, the semi-discrete 5th-order accurate WENO scheme is

$$\frac{dU_{i,j}(t)}{dt} = -\frac{1}{\Delta x}\left(\hat{F}_{i+\frac{1}{2},j} - \hat{F}_{i-\frac{1}{2},j}\right) - \frac{1}{\Delta y}\left(\hat{G}_{i,j+\frac{1}{2}} - \hat{G}_{i,j-\frac{1}{2}}\right) \tag{2.19}$$

with $\hat{F}$ and $\hat{G}$ defined dimension-by-dimension as

$$\hat{F}_{k+\frac{1}{2},j} = \frac{1}{12}(-F_{k-1,j} + 7F_{k,j} + 7F_{k+1,j} - F_{k+2,j})$$

$$+ \sum_{s=1}^{m}\left(-\varphi_N\left(L_s^F \cdot \Delta F_{k-\frac{3}{2},j}^{s,+}, L_s^F \cdot \Delta F_{k-\frac{1}{2},j}^{s,+}, L_s^F \cdot \Delta F_{k+\frac{1}{2},j}^{s,+}, L_s^F \cdot \Delta F_{k+\frac{3}{2},j}^{s,+}\right)\right.$$

$$\left.+ \varphi_N\left(L_s^F \cdot \Delta F_{k+\frac{5}{2},j}^{s,-}, L_s^F \cdot \Delta F_{k+\frac{3}{2},j}^{s,-}, L_s^F \cdot \Delta F_{k+\frac{1}{2},j}^{s,-}, L_s^F \cdot \Delta F_{k-\frac{1}{2},j}^{s,-}\right)\right)R_s^F. \tag{2.20}$$

Here $F_{l,j}^{s,\pm} = \frac{1}{2}(F_{l,j} \pm \alpha^s U_{l,j})$, where $F_{l,j} = F(U_{l,j})$, is the positive/negative part of the flux F at (x_l, y_j). For the global Lax–Friedrichs flux splitting, $\alpha^s = \max_{0 \le p \le N_x} |\lambda_{p,j}^s|$ where $\lambda_{p,j}^s$ is the sth eigenvalue of the Jacobian $\partial F/\partial U$ evaluated at $U_{p,j}$. For the local Lax–Friedrichs splitting, take $\alpha^s = \max_{k-2 \le p \le k+3} |\lambda_{p,j}^s|$. L_s^F and R_s^F are respectively, the sth left and right eigenvector of some mean Jacobian $A_{k+1/2,j}$ depending on $U_{k,j}$ and $U_{k+1,j}$.

Similarly, $\hat{G}$ is given by

$$\hat{G}_{i,k+\frac{1}{2}} = \frac{1}{12}(-G_{i,k-1} + 7G_{i,k} + 7G_{i,k+1} - G_{i,k+2})$$

$$+ \sum_{s=1}^{m}\left(-\varphi_N\left(L_s^G \cdot \Delta G_{i,k-\frac{3}{2}}^{s,+}, L_s^G \cdot \Delta G_{i,k-\frac{1}{2}}^{s,+}, L_s^G \cdot \Delta G_{i,k+\frac{1}{2}}^{s,+}, L_s^G \cdot \Delta G_{i,k+\frac{3}{2}}^{s,+}\right)\right.$$

$$\left.+ \varphi_N\left(L_s^G \cdot \Delta G_{i,k+\frac{5}{2}}^{s,-}, L_s^G \cdot \Delta G_{i,k+\frac{3}{2}}^{s,-}, L_s^G \cdot \Delta G_{i,k+\frac{1}{2}}^{s,-}, L_s^G \cdot \Delta G_{i,k-\frac{1}{2}}^{s,-}\right)\right)R_s^G. \tag{2.21}$$

The quantities are similarly defined, except that here they refer to the flux G in the y direction.

In above, we have provided a WENO semi-discrete approximation, which is 5th-order accurate in terms of local truncation error. Now we provide discretization for the resulting set of ordinary differential equations for time evolution. We can obtain a 5th-order fully discretized scheme if a 5th-order time discretization is used. However, because most of the computational errors come from the spatial discretization, we have employed a 3rd- or 4th-order accurate time evolution scheme. The Runge–Kutta schemes of Shu [25] for the time discretization are used in this paper. Denote the right-hand side of (2.19) as $L(U)$,

omitting the spatial indices; the third-order TVD Runge–Kutta scheme is simply

$$U^{(1)} = U^{(0)} + \Delta t L\left(U^{(0)}\right),$$

$$U^{(2)} = U^{(1)} + \frac{\Delta t}{4}\left(-3L\left(U^{(0)}\right) + L\left(U^{(1)}\right)\right),$$

$$U^{(3)} = U^{(2)} + \frac{\Delta t}{12}\left(-L\left(U^{(0)}\right) - L\left(U^{(1)}\right) + 8L\left(U^{(2)}\right)\right).$$

A useful 4th-order, but not TVD, Runge–Kutta scheme is

$$U^{(1)} = U^{(0)} + \frac{\Delta t}{2}L\left(U^{(0)}\right),$$

$$U^{(2)} = U^{(1)} + \frac{\Delta t}{2}\left(-L\left(U^{(0)}\right) + L\left(U^{(1)}\right)\right),$$

$$U^{(3)} = U^{(2)} + \frac{\Delta t}{2}\left(-L\left(U^{(1)}\right) + 2L\left(U^{(2)}\right)\right),$$

$$U^{(4)} = U^{(3)} + \frac{\Delta t}{6}\left(L\left(U^{(0)}\right) + 2L\left(U^{(1)}\right) - 4L\left(U^{(2)}\right) + L\left(U^{(3)}\right)\right).$$

In all our numerical tests in Section 3, we have used the 4th-order Runge–Kutta scheme for time evolution.

2.3. The Eigenvectors for the MHD Equations

We first present the eigen-system for the one-dimensional MHD system,

$$U_t = -F(U)_x \tag{2.22}$$

with

$$U = (\rho,\ \rho v_x,\ \rho v_y,\ \rho v_z,\ B_y,\ B_z,\ \varepsilon)^\top, \tag{2.23}$$

$$F(U) = \left(\rho v_x,\ \rho v_x^2 + p^*,\ \rho v_x v_y - B_x B_y,\ \rho v_x v_z - B_x B_z,\ v_x B_y - v_y B_x,\right.$$

$$\left. v_x B_z - v_z B_x,\ v_x(\varepsilon + p^*) - B_x(v_x B_x + v_y B_y + v_z B_z)\right)^\top. \tag{2.24}$$

Here $p^* = p + \frac{1}{2}B^2$ and $\varepsilon = \frac{1}{2}\rho v^2 + \frac{1}{2}B^2 + p/(\gamma - 1)$. Note that the subscripts for **B**, **v**, and other similar variables refer to the components of the variables and do not indicate the spatial derivatives as in (2.22).

Let $(b_x, b_y, b_z) = (B_x, B_y, B_z)/\sqrt{\rho}$, $b^2 = b_x^2 + b_y^2 + b_z^2$ and $b_\perp^2 = b_y^2 + b_z^2$. The sound speed and the Alfvén speed are, respectively,

$$a = \sqrt{\frac{\gamma p}{\rho}}, \qquad c_a = |b_x|.$$

The fast and slow speeds are given by

$$C_{f,s} = \left\{\frac{1}{2}\left[a^2 + b^2 \pm \sqrt{(a^2 + b^2)^2 - 4a^2 b_x^2}\right]\right\}^{\frac{1}{2}}.$$

The eigen-system of (2.22) has extensively been studied; see, for example, Jeffrey and Taniuti [13]. However, the set of eigenvectors given there can be singular at the points where the eigenvalues are degenerate. Brio and Wu [4] have given a proper choice of normalization that avoids these singularities and provides a complete set of eigenvectors. Their procedure is employed in this work. To this end, we define

$$(\beta_y, \beta_z) = \begin{cases} \frac{(B_y, B_z)}{\sqrt{B_y^2 + B_z^2}} & \text{if } B_y^2 + B_z^2 \neq 0, \\ \left(\frac{1}{\sqrt{2}}, \frac{1}{\sqrt{2}}\right) & \text{otherwise}, \end{cases} \tag{2.25}$$

$$(\alpha_f, \alpha_s) = \begin{cases} \frac{\left(\sqrt{a^2 - c_s^2}, \sqrt{c_f^2 - a^2}\right)}{\sqrt{c_f^2 - c_s^2}} & \text{if } B_y^2 + B_z^2 \neq 0 \text{ or } \gamma p \neq B_x^2, \\ \left(\frac{1}{\sqrt{2}}, \frac{1}{\sqrt{2}}\right) & \text{otherwise}, \end{cases} \tag{2.26}$$

$$\text{sgn}(B_x) = \begin{cases} 1 & \text{if } B_x \geq 0, \\ -1 & \text{otherwise}. \end{cases} \tag{2.27}$$

The eigenvalues are

$$\lambda_{1,7} = v_x \mp c_f, \qquad \lambda_{2,6} = v_x \mp c_a, \qquad \lambda_{3,5} = v_x \mp c_s, \qquad \lambda_4 = v_x.$$

With the abbreviations,

$$\gamma_1 = \frac{\gamma - 1}{2},$$

$$\gamma_2 = \frac{\gamma - 2}{\gamma - 1},$$

$$\tau = \frac{\gamma - 1}{a^2},$$

$$\Gamma_f = \alpha_f c_f v_x - \alpha_s c_s \, \text{sgn}(B_x)(\beta_y v_y + \beta_z v_z),$$

$$\Gamma_a = \text{sgn}(B_x)(\beta_z v_y - \beta_y v_z),$$

$$\Gamma_s = \alpha_s c_s v_x + \alpha_f c_f \, \text{sgn}(B_x)(\beta_y v_y + \beta_z v_z),$$

the corresponding left and right eigenvectors are given by

$$L_{1,7} = \frac{1}{2a^2} \Big(\gamma_1 \alpha_f v^2 \pm \Gamma_f, (1 - \gamma)\alpha_f v_x \mp \alpha_f c_f, (1 - \gamma)\alpha_f v_y \pm c_s \alpha_s \beta_y \, \text{sgn}(B_x),$$

$$(1 - \gamma)\alpha_f v_z \pm c_s \alpha_s \beta_z \, \text{sgn}(B_x), (1 - \gamma)\alpha_f B_y - \sqrt{\rho} a \alpha_s \beta_y,$$

$$(1 - \gamma)\alpha_f B_z - \sqrt{\rho} a \alpha_s \beta_z, (\gamma - 1)\alpha_f \Big),$$

$$R_{1,7}^\top = \Big(\alpha_f, \alpha_f (v_x \mp c_f), \alpha_f v_y \pm c_s \alpha_s \beta_y \, \text{sgn}(B_x), \alpha_f v_z \pm c_s \alpha_s \beta_z \, \text{sgn}(B_x),$$

$$\frac{a \alpha_s \beta_y}{\sqrt{\rho}}, \frac{a \alpha_s \beta_z}{\sqrt{\rho}}, \alpha_f \left[\frac{1}{2} v^2 + c_f^2 - \gamma_2 a^2 \right] \mp \Gamma_f \Big),$$

$$L_{2,6} = \frac{1}{2} \Big(\Gamma_a, 0, -\beta_z \, \text{sgn}(B_x), \beta_y \, \text{sgn}(B_x), \mp\sqrt{\rho}\beta_z, \pm\sqrt{\rho}\beta_y, 0 \Big),$$

$$R_{2,6}^\top = \left(0, 0, -\beta_z \operatorname{sgn}(B_x), \beta_y \operatorname{sgn}(B_x), \mp\frac{\beta_z}{\sqrt{\rho}}, \pm\frac{\beta_y}{\sqrt{\rho}}, -\Gamma_a\right),$$

$$L_{3,5} = \frac{1}{2a^2}\left(\gamma_1\alpha_s v^2 \pm \Gamma_s, (1-\gamma)\alpha_s v_x \mp \alpha_s c_s, (1-\gamma)\alpha_s v_y \mp c_f\alpha_f\beta_y \operatorname{sgn}(B_x),\right.$$
$$(1-\gamma)\alpha_s v_z \mp c_f\alpha_f\beta_z \operatorname{sgn}(B_x), (1-\gamma)\alpha_s B_y - \sqrt{\rho}a\alpha_f\beta_y,$$
$$\left.(1-\gamma)\alpha_s B_z - \sqrt{\rho}a\alpha_f\beta_z, (\gamma-1)\alpha_s\right),$$

$$R_{3,5}^\top = \left(\alpha_s, \alpha_s(v_x \mp c_s), \alpha_s v_y \mp c_f\alpha_f\beta_y \operatorname{sgn}(B_x), \alpha_s v_z \mp c_f\alpha_f\beta_z \operatorname{sgn}(B_x),\right.$$

$$\left.-\frac{a\alpha_f\beta_y}{\sqrt{\rho}}, -\frac{a\alpha_f\beta_z}{\sqrt{\rho}}, \alpha_s\left[\frac{1}{2}v^2 + c_s^2 - \gamma_2 a^2\right] \mp \Gamma_s\right),$$

$$L_4 = \left(1 - \frac{1}{2}\tau v^2, \tau v_x, \tau v_y, \tau v_z, \tau B_y, \tau B_z, -\tau\right),$$

$$R_4^\top = \left(1, v_x, v_y, v_z, 0, 0, \frac{1}{2}v^2\right),$$

where $R^\top$ denotes the transpose of a column vector R.

In the actual implementation, the condition $B_x^2 + B_y^2 \neq 0$ in (2.25) and (2.26) is relaxed to $B_x^2 + B_y^2 > \delta B^2$ with δ being a small dimensionless constant, about 10^{-12}. Likewise, the condition $\gamma p \neq B_x^2$ is relaxed to $|\gamma p - B_x^2| > \delta\gamma p$.

To evaluate L_s and R_s ($s = 1, 2, \ldots, 7$) at the half grid point $k + \frac{1}{2}$, a state vector is required there. We define this state as the arithmetic averaging of the values at the two neighboring grid points k and $k + 1$ for the density, the velocity, the magnetic field, and the hydrodynamic pressure. Although it is possible to define the state at $k + \frac{1}{2}$ through Roe averaging, tests show little differences whether a simple averaging or a Roe average is used for time-dependent problems. For $\gamma = 2$, a single Roe-average state can be obtained. In the general situation, however, more than one average of the magnetic-field components is necessary to achieve Roe-averaging [20].

For the 2D MHD system, which is (2.18) with

$$U = (\rho, \rho v_x, \rho v_y, \rho v_z, B_x, B_y, B_z, \varepsilon)^\top, \tag{2.28}$$

$$F(U) = \left(\rho v_x, \rho v_x^2 + p^* - B_x^2, \rho v_x v_y - B_x B_y, \rho v_x v_z - B_x B_z, 0, v_x B_y - v_y B_x,\right.$$
$$\left.v_x B_z - v_z B_x, v_x(\varepsilon + p^*) - B_x(v_x B_x + v_y B_y + v_z B_z)\right)^\top, \tag{2.29}$$

$$G(U) = \left(\rho v_y, \rho v_y v_x - B_y B_x, \rho v_y^2 + p^* - B_y^2, \rho v_y v_z - B_y B_z,\right. \tag{2.30}$$
$$v_y B_x - v_x B_y, 0, v_y B_z - v_z B_y,$$
$$\left.v_y(\varepsilon + p^*) - B_y(v_x B_x + v_y B_y + v_z B_z)\right)^\top, \tag{2.31}$$

its eigen-system can be found by slightly modifying the eigen-system for the one-dimensional MHD equations. First we notice the similarity between the fluxes F and G. In fact, $G(U) = SF(SU)$ where S is a "swap" matrix which swaps the 2nd component of a vector with its 3rd component and at the same time, swaps the 5th component with the 6th component, i.e., $S_{23} = S_{32} = S_{56} = S_{65} = 1$ and the rest of entries are zero. This property can be used to find the eigen-system of G from the eigen-system of F.

We have experimented with two sets of eigenvectors for the eigen-system of F: One is a direct extension of the one-dimensional system and the other is based on the modification proposed by Powell *et al.* [20]. In the direct extension, we first notice that the 5th component of F is zero, which corresponds to the evolution equation for the x-component of the magnetic field B_x. If we ignore this component, the rest is identical to the one-dimensional flux, in which case B_x is a constant. In this case, L_s^F and R_s^F ($s = 1, 2, \ldots, 7$) can be obtained in the same way as in the one-dimensional case. We call such an eigen-system the 7×7 eigen-system.

In the 8×8 eigen-system of Powell *et al.* [20], the eigenvalues are

$$\lambda_{1,8} = v_x \mp c_f, \qquad \lambda_{2,7} = v_x \mp c_a, \qquad \lambda_{3,6} = v_x \mp c_s, \qquad \lambda_{4,5} = v_x.$$

Their corresponding eigenvectors can be obtained from the 7×7 eigen-system in a simple manner. The left eigenvectors $L_{1,8}$, $L_{2,7}$, $L_{3,6}$, and L_4 are obtained, respectively, by inserting into $L_{1,7}$, $L_{2,6}$, $L_{3,5}$, and L_4 of the 7×7 eigen-system a 5th component whose value is $-B_x$ multiplied by the last component of each left eigenvector. Similarly, the right eigenvectors $R_{1,8}$, $R_{2,7}$, $R_{3,6}$, and R_4 are obtained, respectively, by adding a 5th component with null value to $R_{1,7}$, $R_{2,6}$, $R_{3,5}$, and R_4 of the 7×7 eigen-system. In addition, L_5 and R_5 are given by

$$L_5 = (0, 0, 0, 0, 1, 0, 0, 0),$$
$$R_5^\top = (0, 0, 0, 0, 1, 0, 0, B_x).$$

As in the 7×7 eigen-system, the values of L_s and R_s ($s = 1, 2, \ldots, 8$) at $(k + \frac{1}{2}, j)$ are obtained at the half-grid-point state, whose values are the arithmetic averaging of density, velocity, the magnetic field, and pressure at grid points (k, j) and $(k + 1, j)$. Except for the 5th component, the 7×7 and 8×8 eigen-systems give same numerical fluxes $\hat{F}_{k+\frac{1}{2}, j}$. The 5th component can be nonzero in the 8×8 system and is zero in the 7×7 system.

3. NUMERICAL RESULTS

We present in this section the test results of the WENO MHD scheme for several one-dimensional and two-dimensional test problems. In all tests, we have used the 4th-order Runge–Kutta scheme for time discretization and the global Lax–Friedrichs flux splitting. The time step size for one-dimensional problems is given dynamically by

$$\Delta t = \frac{0.8 \, \Delta x}{\max(|v_x| + c_f)}, \tag{3.1}$$

where the maximum is taken over all computational grid points. For two-dimensional problems, it is determined every time step by

$$\Delta t = 0.8 \left/ \left[\frac{\max(|v_x| + c_f^x)}{\Delta x} + \frac{\max(|v_y| + c_f^y)}{\Delta y} \right] \right., \tag{3.2}$$

where the maxima are also taken over all computational grid points. Here c_f^x and c_f^y are the fast speeds in the x- and y-direction, respectively. The CFL number is 0.8.

3.1. *One-Dimensional Riemann Problems*

We solve the one-dimensional MHD equations (2.22)–(2.24) with the following two Riemann data, both drawn from [4]. The first Riemann problem is given by

$$(\rho, v_x, v_y, v_z, B_y, B_z, p) = \begin{cases} (1.000, \ 0, \ 0, \ 0, \ +1, \ 0, \ 1.0) & \text{for } x < 0, \\ (0.125, \ 0, \ 0, \ 0, \ -1, \ 0, \ 0.1) & \text{for } x > 0, \end{cases}$$

with $B_x = 0.75$, $\gamma = 2$. Note that the hydrodynamic data are the same as the Sod's Riemann problem [28]. This is the example used by Brio and Wu [3, 4] to show the formation of a compound wave in MHD.

We take the computational domain to be $[-1, 1]$ with 800 points. The solution at $t = 0.2$ is shown in Fig. 2, which includes, moving to the left, a fast rarefaction wave, an intermediate
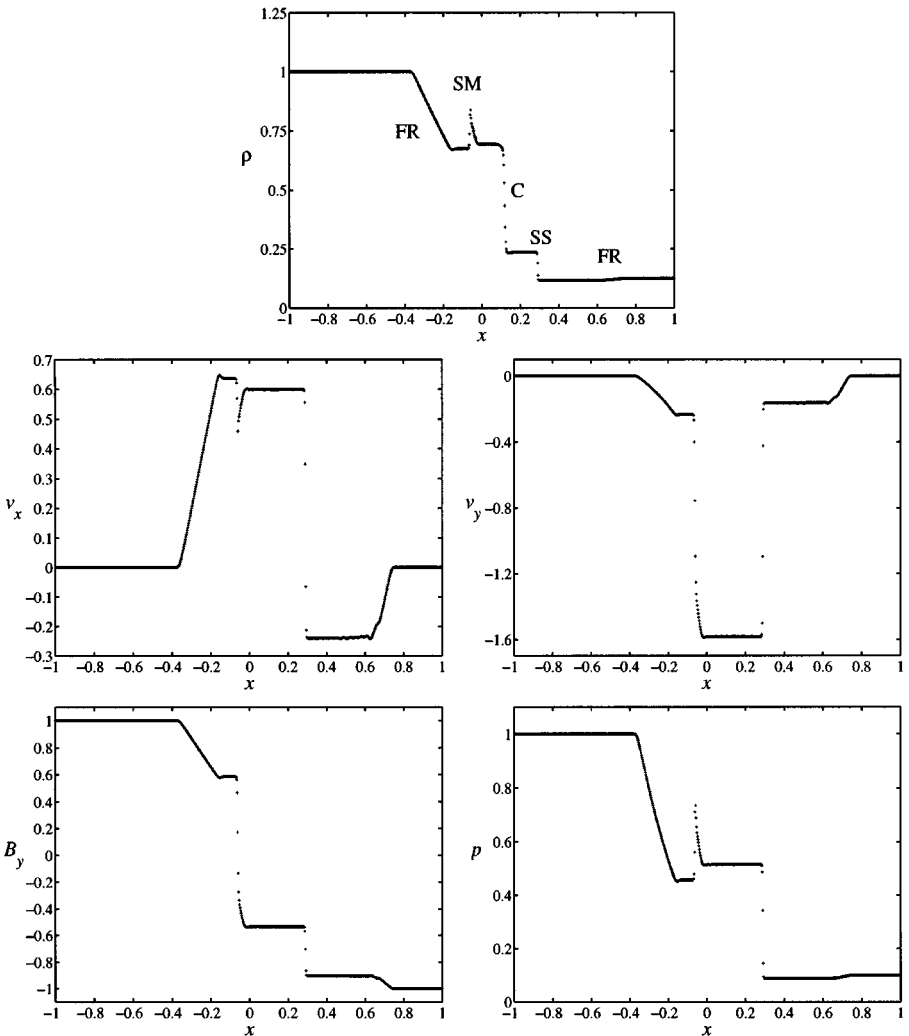

FIG. 2. The first Riemann problem of Brio and Wu with 800 grid points at $t = 0.2$. The symbol *FR* denotes a fast rarefaction wave; *SM* is a compound wave (an intermediate shock followed by a slow rarefaction wave); *C* is a contact discontinuity; *SS* is a slow shock.

shock, which is attached by a slow rarefaction wave, and, moving to the right, a contact discontinuity, a slow shock, and a fast rarefaction wave. The left-moving intermediate shock, which changes B_y from 0.58 to -0.31, is of the type that its shock-frame flow speed is sub-fast, super-Alfvénic, and super-slow upstream and sub-Alfvénic, and equal to slow speed downstream. Thus the intermediate shock is attached by the slow rarefaction wave, which changes B_y from -0.31 to -0.53, and both form a compound wave. Across this compound wave, there is only one parameter to specify. Therefore we get a five parameter family of states which can be connected to the left state. Since there are five values (ρ, v_x, v_y, B_y, and p) to determine for the right state, the Riemann solution of this problem is unique. In this example we are confined to a planar situation, where $B_z = v_z = 0$, so the intermediate shock structure is uniquely defined and multiple Riemann solutions mentioned in the Introduction do not occur. If B_z and/or v_z are nonzero, then more than one Riemann solution can occur [33].

The computed result agrees with the one obtained by Brio and Wu [4], who used a second order TVD scheme. Since around shock waves and discontinuities, our code becomes first-order accurate, just like their code, we do not expect any improvement in capturing these structures. Indeed, our result shows that there are 4 to 5 grid points within each shock layer, which is comparable with theirs. For the rarefaction waves, our results also agree with theirs. Since the solution is so simple, our high-order code does not make any obvious change either. However, our result shows noticeable oscillations near the trailing edge of the right-moving fast rarefaction wave, which may be caused by the high-order approximation. Such oscillations disappear when we compute the same problem in a moving frame.

This 1D Riemann problem is also solved in a 2D computational grid, serving as a test for the 2D version of the code. A grid of 600×600 points covering $[-1, 1] \times [-1, 1]$ in the (x, y) plane is used. In a $45°$-rotated coordinate (x', y'), the Riemann data are prescribed initially for $x' > 0$ and $x' < 0$ regions. Figure 3 shows the results of two calculations plotted along the x' direction. Both computations use the 8×8 eigen-system. The left-hand column of the figure shows the results that include the additional step of enforcing the $\nabla \cdot \mathbf{B} = 0$ condition as specified in the Introduction. A relaxation method is employed in solving the Poisson equation. The right-hand column contains results without this correction procedure. Clearly the correction step plays an important role in these 2D calculations. The one with the correction step agrees with the 1D results in Fig. 2. Without the correction, the results show spurious oscillations near the slow rarefaction wave within the compound wave.

The second Riemann problem is

$$(\rho, v_x, v_y, v_z, B_y, B_z, p) = \begin{cases} (1.000, \ 0, \ 0, \ 0, \ +1, \ 0, \ 1000) & \text{for } x < 0, \\ (0.125, \ 0, \ 0, \ 0, \ -1, \ 0, \ 0.10) & \text{for } x > 0, \end{cases}$$

with $B_x = 0$, $\gamma = 2$. This problem is used to evaluate the code for high Mach number flow. The Mach number corresponding to the right-moving shock wave is 15.5. If one replaces the hydrodynamic pressure by the sum of the plasma and the magnetic pressures, this problem becomes a standard hydrodynamical Riemann problem and thus the exact solution can be easily found. In addition, the equation for B_y is the same as the equation for the density. Thus, B_y and ρ behave similarly to the left and to the right of the tangential discontinuity, where the jumps in B_y and ρ are not related. We take the computational domain to be $[-1, 1]$ with 200 points. The solution at $t = 0.012$ is shown in Fig. 4, with the exact solution shown by a solid continuous line. The quality of the solution is again very similar to that of
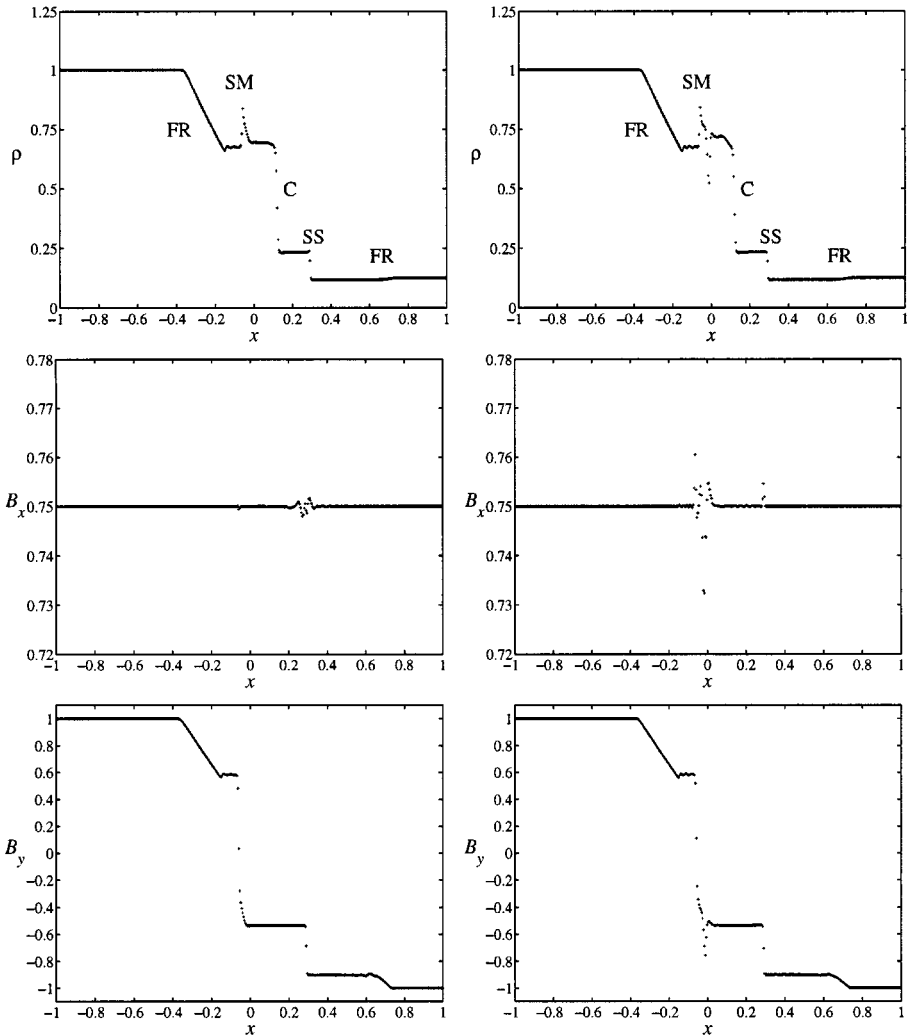
FIG. 3. The first Riemann problem of Brio and Wu computed in a 2D grid with 600×600 points at $t = 0.2$. The left-hand column shows the results with the correction step of enforcing the condition of $\nabla \cdot \mathbf{B} = 0$, while the right-hand column contains results without this step.

the TVD scheme. There are about 5 points within the strong shock and about seven points within the tangential discontinuity. Note that in our code, no artificial compression is used to sharpen the tangential discontinuity.

3.2. *Formation of Intermediate Shocks*

In this example, we repeat the calculation of Wu [32], that showed that intermediate shocks can be formed through nonlinear wave steepening from continuous waves, indicating that intermediate shocks are physical. As in [32], a slow simple wave solution is used as an initial condition. Initially $B_y(x) = 0.5 \sin(2\pi x)$ over $0 \leq x \leq 1$ with a periodic boundary condition. The other quantities (ρ, v_x, v_y, v_z, B_z, and p) are numerically obtained by solving the simple wave relation: $dU = R_5$, with U given in (2.23) and R_5, given in Subsection 2.3, the right-eigenvector for the slow wave characteristic speed $v_x + c_S$. All quantities are normalized
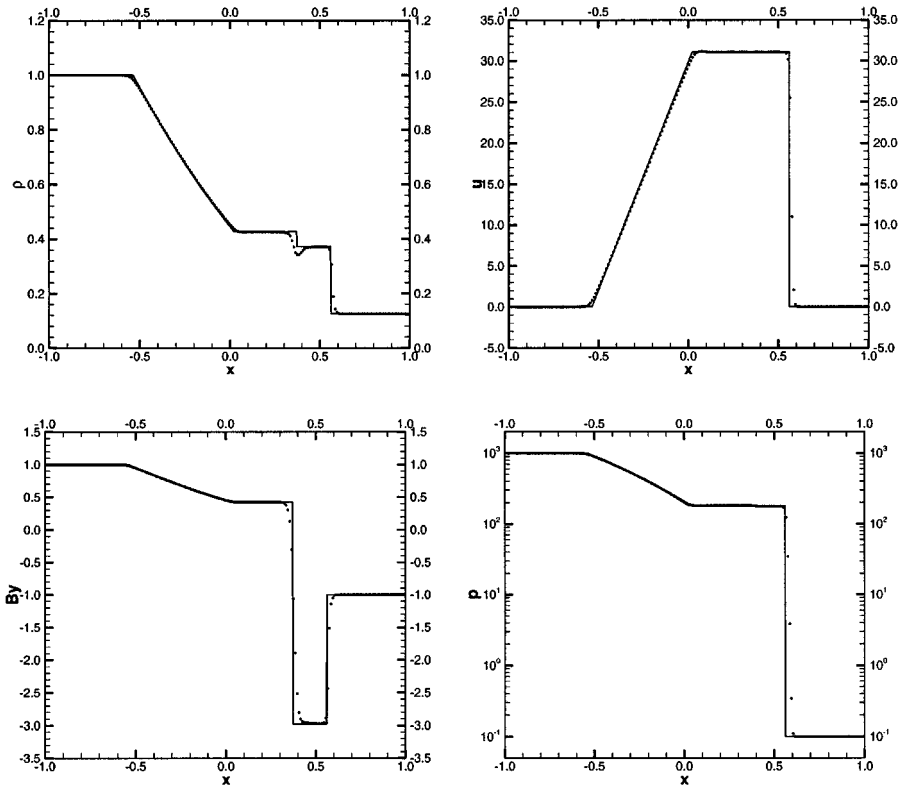
FIG. 4. The second Riemann problem of Brio and Wu with 200 grid points at $t = 0.012$.

with the following values at $B_y = 0$: $B_x = 1$, $\rho = 1$, $p = 1$, $v_x = v_y = v_z = 0$, and $B_z = 0$. The ratio of specific heats $\gamma = 5/3$ is used. In this one-dimensional problem, B_x is a constant and both v_z and B_z vanish; it is a planar problem.

Figure 5 shows the ρ and B_y solutions at $t = 0$, 0.5, 0.6, and 1, which are obtained with the new WENO code using 2560 grid points. These results agree with the results in [32], where plots for other variables and results at later times can be found. Initially, the wave is compressive in the range $0.25 \geq x \geq 0$ and $0.75 \geq x \geq 0.5$, where $|B_y|$ decreases from 0.5 to 0 as ρ increases from 0.81 to 1. The wave is expansive in the other intervals. At $B_y = 0$, the slow wave and the intermediate wave are degenerate and also the system is non-convex there. Thus this calculation seems to be a good example to test the accuracy of the codes. As the solution evolves, the characteristics in the compressive regions begin to converge while those in the expansive regions spread. As shown in [32], a pair of slow shocks is first formed at $t \sim 0.54$ at $x \sim 0.13$ and 0.63, whose characteristics can be traced back to the initial location at $x = 0.63$ and 0.13, respectively, where the steepening rate is maximum. Thus prior to $t \sim 0.54$, the solution is smooth and the codes should attain their expected accuracy. The evolution continues after the shock formation. The slow characteristics and, eventually, the intermediate wave characteristics converge into the shocks. At $t = 1$, the shocks evolve into intermediate shocks: B_y changes its sign and jumps from -0.47 to 0.029 across the shock at $x \sim 0.49$ and from 0.47 to -0.029 across the one at $x \sim 0.99$. After the shock formation, fast waves, the entropy wave, and the other slow wave (moving with $v_x - c_s$) begin to form. These waves are not necessarily smooth. They travel through this periodic system and ultimately determine the order of accuracy of the calculation.
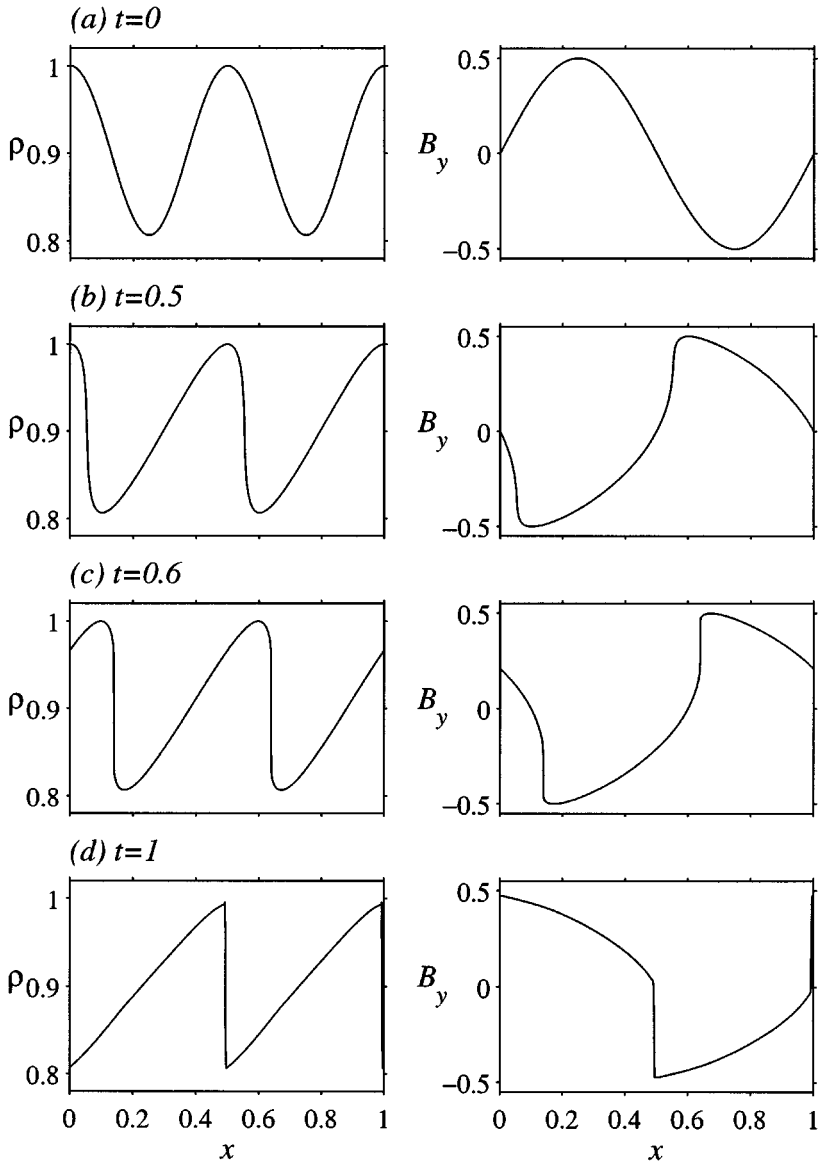
FIG. 5. Formation of intermediate shocks: Plots of ρ and B_y at $t = 0$, 0.5, 0.6, and 1. Slow shocks are first formed at $t \sim 0.54$ and they evolve into intermediate shocks at $t \sim 1$.

In Table I, we show the errors of two schemes at $t = 0.25$. In addition to the new WENO MHD scheme, we include a second scheme which uses a 3rd-order ENO scheme [27] (3rd-order accurate in space and time). Both ENO and WENO share the same construction. Their differences are in the choice of the flux and the order of the Runge–Kutta time integration. For the WENO scheme, we have adjusted the time step to $\Delta t \sim (\Delta x)^{5/4}$ so that the 4th-order Runge–Kutta procedure in time is effectively 5th-order [14]. The errors are the deviations of B_y away from its values computed with the WENO code using 2560 grid points. The WENO scheme gives an order of accuracy of about 4.5 with 80–320 grid points while the ENO scheme achieves an order of about 2.5.

TABLE I

Accuracy on the Example in Subsection 3.2 at $t = 0.25$ with a 5th-Order WENO Scheme and a 3rd-Order ENO Scheme

Method	N	L_1 error	L_1 order	L_∞ error	L_∞ order
WENO	10	2.8e-2	—	5.3e-2	—
	20	5.3e-3	2.4	1.9e-2	1.5
	40	5.1e-4	3.4	2.6e-3	2.9
	80	2.8e-5	4.2	2.9e-4	3.2
	160	1.2e-6	4.5	1.2e-5	4.6
	320	4.3e-8	4.8	4.5e-7	4.7
ENO	10	3.0e-2	—	6.3e-2	—
	20	8.0e-3	1.9	2.0e-2	1.7
	40	1.3e-3	2.6	4.7e-3	2.1
	80	2.2e-4	2.6	1.1e-3	2.1
	160	3.8e-5	2.5	2.2e-4	2.3
	320	7.8e-6	2.3	7.0e-5	1.7

In Table II, the errors are shown at $t = 0.5$, when the wave is highly steepened but still before the shock formation. Near the steepened regions, the codes are expected to be less accurate. The L_1 and L_∞ errors confirm this trend. We expect both L_1 and L_∞ to reach their expected order of accuracy as the number of grid points is increased. However, the codes still obtain their expected accuracy in the region away from these steepened intervals as shown by L_1^* errors, which are the L_1 errors limited to the interval within $0.2 \leq x \leq 0.4$.

The errors at $t = 0.6$, after shocks are formed, are presented in Table III. Because of the shocks, the L_1 order is about 1 for both schemes. As the shocks are formed, other waves (including entropy, fast, and intermediate waves) are necessarily generated. In the region that is not yet affected by these waves, high order of accuracy is maintained, as indicated by the L_1^* errors which covers $0.3 \leq x \leq 0.4$. By the time $t = 1$ (Table IV), these other waves

TABLE II

Accuracy on the Example in Subsection 3.2 at $t = 0.5$ with a 5th-Order WENO Scheme and a 3rd-Order ENO Scheme

Method	N	L_1 error	L_1 order	L_1^* error	L_1^* order	L_∞ error	L_∞ order
WENO	10	5.8e-2	—	2.6e-2	—	1.2e-1	—
	20	1.8e-2	1.9	3.0e-3	3.1	6.4e-2	0.91
	40	7.4e-3	1.3	3.2e-4	3.2	4.6e-2	0.48
	80	2.6e-3	1.5	1.9e-5	4.1	3.8e-2	0.28
	160	7.4e-4	1.8	6.7e-7	4.8	2.3e-2	0.72
	320	1.6e-4	2.2	4.5e-9	7.2	7.6e-3	1.6
ENO	10	6.8e-2	—	2.2e-2	—	1.4e-1	—
	20	2.2e-2	1.6	3.7e-3	2.6	6.8e-2	1.0
	40	1.0e-2	1.1	7.6e-4	2.3	5.1e-2	0.42
	80	4.0e-3	1.3	1.6e-4	2.2	3.9e-2	0.39
	160	1.3e-3	1.6	2.7e-5	2.6	2.4e-2	0.70
	320	3.5e-4	1.9	4.7e-6	2.5	1.1e-2	1.1

Note. L_1 and L_∞ cover $0 \leq x \leq 1$ while L_1^* covers only $0.2 \leq x \leq 0.4$.

TABLE III
Accuracy on the Example in Subsection 3.2 at $t = 0.6$ with a 5th-Order WENO Scheme and a 3rd-Order ENO Scheme

Method	N	L_1 error	L_1 order	L_1^* error	L_1^* order	L_∞ error
WENO	20	3.3e-2	—	4.5e-3	—	1.4e-1
	40	1.4e-2	1.2	8.1e-4	2.5	1.0e-1
	80	5.1e-3	1.5	1.2e-4	2.8	7.9e-2
	160	2.9e-3	0.81	5.4e-6	4.5	1.1e-1
	320	1.4e-3	1.1	4.9e-7	3.5	8.6e-2
ENO	20	4.1e-2	—	1.4e-4	—	1.6e-1
	40	1.8e-2	1.2	1.2e-3	—	1.1e-1
	80	8.2e-3	1.1	4.0e-4	1.6	1.1e-1
	160	3.9e-3	1.1	1.0e-4	2.0	1.1e-1
	320	1.8e-3	1.1	2.1e-5	2.3	8.6e-2

Note. L_1 and L_∞ cover $0 \le x \le 1$ while L_1^* covers only $0.3 \le x \le 0.4$.

have traveled throughout the system. The L_1 order is again about 1. In the regions away from the intermediate shocks, the solution is not exactly smooth because these other waves, though small in amplitude, are not necessarily smooth. This seems to explain the fact that the L_1^* order over the $0.2 \le x \le 0.3$ region drops to about 1 as the L_1^* errors become small. Although both WENO and ENO have similar orders of accuracy at $t = 1$, Fig. 6 shows that WENO provides a better shock capturing capability than both ENO and a 2nd-order scheme by Liu and Lax [16]. The Liu–Lax scheme (labelled LL; 2nd-order accurate in space and time) shares the same construction as WENO and ENO but has a different choice of the flux and the order of the Runge–Kutta time integration.

3.3. *Two-Dimensional Kelvin–Helmholtz Instability*

The Kelvin–Helmholtz instability can arise when two superposed fluids flow one over the other with a relative velocity. It occurs in many physical phenomena. As an example, the Kelvin–Helmholtz instability is considered as an important mechanism for the momentum

TABLE IV
Accuracy on the Example in Subsection 3.2 at $t = 1$ with a 5th-Order WENO Scheme and a 3rd-Order ENO Scheme

Method	N	L_1 error	L_1 order	L_1^* error	L_1^* order	L_∞ error
WENO	20	4.6e-2	—	7.8e-3	—	2.0e-1
	40	2.2e-2	1.1	1.7e-3	2.2	1.7e-1
	80	1.1e-2	1.0	4.1e-4	2.1	1.7e-1
	160	3.1e-3	1.8	2.2e-4	0.9	8.8e-2
	320	1.5e-3	1.0	1.1e-4	1.0	8.8e-2
ENO	20	5.9e-2	—	1.1e-2	—	2.4e-1
	40	2.8e-2	1.1	3.5e-3	1.7	2.0e-1
	80	1.3e-2	1.1	5.4e-4	2.7	1.7e-1
	160	4.3e-3	1.6	2.1e-4	1.4	1.0e-1
	320	2.1e-3	1.0	1.2e-4	0.8	1.1e-1

Note. L_1 and L_∞ cover $0 \le x \le 1$ while L_1^* covers only $0.2 \le x \le 0.3$.
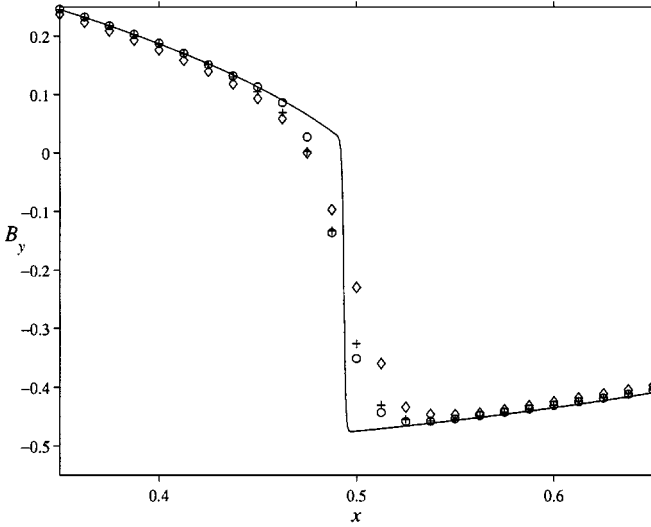
FIG. 6. The B_y distributions across an intermediate shock at $x \sim 0.49$ at $t = 1$. The solid curve is obtained by the WENO scheme with 2560 grid points. Results marked by $\bigcirc$, $+$, and $\diamond$ are obtained with 80 grid points from the WENO code, the 3rd-order ENO code, and the 2nd-order Liu–Lax scheme, respectively.

transfer at the Earth's magnetopause boundary, which separates the solar wind flow from the Earth's magnetosphere. Here we apply the WENO scheme to the two-dimensional periodic model and convective model with transverse magnetic field configuration. In a convective model, the excitation has a finite convective velocity. See [31] and its references for details.

The governing equations are the two-dimensional MHD system (2.18), (2.28)–(2.31). The initial stationary configuration of the periodic model is given by $\rho_0 = 1$, $v_{x0} = (v_0/2)$ $\tanh(y/a)$, $v_{y0} = v_{z0} = 0$, $B_{x0} = B_{y0} = 0$, $B_{z0} = 1$, and $p_0 = 0.5$, where a denotes the width of the velocity shear layer. At $t = 0$, a small perturbation of the following form is introduced:

$$\tilde{v}_{x0} = \begin{cases} -\tilde{v}_0 \sin(2\pi x/\lambda)/(1 + y^2), & \text{if } -\frac{\lambda}{2} < x < \frac{\lambda}{2}, \\ 0, & \text{otherwise.} \end{cases} \tag{3.3}$$

The computational domain is $[-\frac{L}{2}, \frac{L}{2}] \times [0, H]$. We have used $v_0 = 2$, $\tilde{v}_0 = 0.008$, $L = \lambda = 5\pi$, $H = 10$, $a = 1$, and $\gamma = 2$. The periodic boundary condition is used in the x-direction. The free outflow condition is applied at the top boundary at $y = H$. Here we only compute half of the flow, the other half, from $y = -H$ to $y = 0$, can be obtained by symmetry conditions that under the transformation $\mathbf{x} \to -\mathbf{x}$, ρ, p, and B_z are symmetric and v_x and v_y are antisymmetric [31]. We have used two grids in the calculations: one has 48×30 grid points and the other has 96×60 grid points. The grids are stretched in the y-direction with a Roberts transformation

$$y \leftarrow \frac{H \sinh(\tau y/2H)}{\sinh(\tau/2)} \tag{3.4}$$

with $\tau = 6$. This transform renders a denser grid near $y = 0$, where much of the action is taking place and a coarser grid near $y = H$, where little is happening. The time evolution
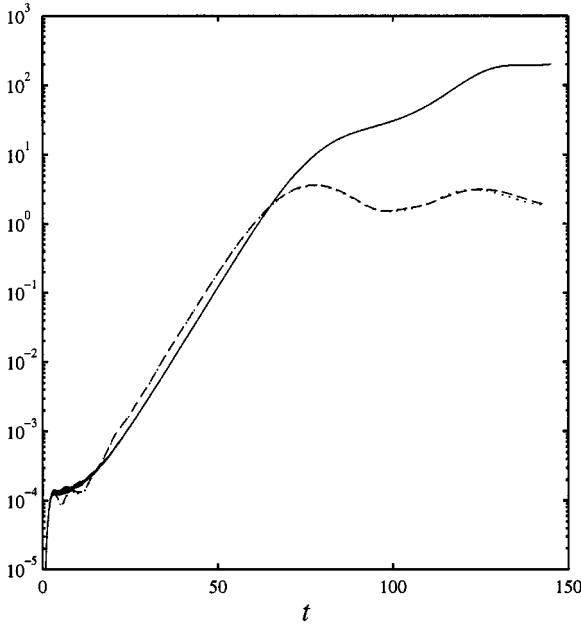
FIG. 7.   Time evolution of the total transverse kinetic energy integrated over $[-L/2, L/2] \times [-H, H]$ for both periodic and convective Kelvin–Helmholtz instability. The results from the periodic systems with 48×30 grid points and with 96×60 grid points are shown by a dashed curve and a dotted curve, respectively. The convective system is given in a solid curve. For $20 < t < 50$, the transverse kinetic energy grows like $e^{2\gamma t}$ with γ, the linear growth rate, equal to 0.09.

of the total transverse kinetic energy integrated over $[-5\pi/2, 5\pi/2] \times [-10, 10]$ for both grids is shown in Fig. 7. The two calculations show almost identical growth. In Fig. 8, we show the flow components at $t = 144$. The calculation with the fine grid clearly captures the weak shock near the left boundary while, as expected, the shock has a greater spread in the coarse-grid run. The shock forms because of the creation of the vortex flow. To the flow outside the vortex, the situation is similar to the flow over an airfoil in aerodynamics, where shock waves can be generated off the airfoil.

For the convective model, we assume the same initial profile as in the periodic model. By using the velocity profile of $v_{x0} = (v_0/2) \tanh(y/a)$, we carry out the calculation in a frame that moves with the excitation of the instability. However, in contrast to the periodic model, the convective model does not impose the periodic boundary condition in the x-direction. Instead, a large computational domain $(L \gg \lambda)$ is employed to allow the excitation to convect freely. With a sufficiently large value of L, no disturbance can reach the boundaries at $x = \pm L/2$ during the course of the calculation. Since the size of vortices formed in the convective system is larger than that of the periodic model, the computational domain in the y direction is also increased. As in [31], we use $L = 11\lambda = 55\pi$, $H = 20$, and $a = 1$. The initial excitation is imposed in the region $-(\lambda/2) < x < (\lambda/2)$ given by (3.3) with $\tilde{v}_0 = 0.008$. A grid of 528×48 points, with the same grid transform in the y-direction as that in (3.4), is used to achieve comparable resolution with that of the periodic system. The time evolution of the transverse kinetic energy is shown in Fig. 7. As in [31], we observe that the transverse kinetic energy continues to grow long after the saturation for the periodic system. We also observe the formation of large vortices, whose size can be nearly two times larger than the initial perturbation wave-length. The shocks formed off these vortices are
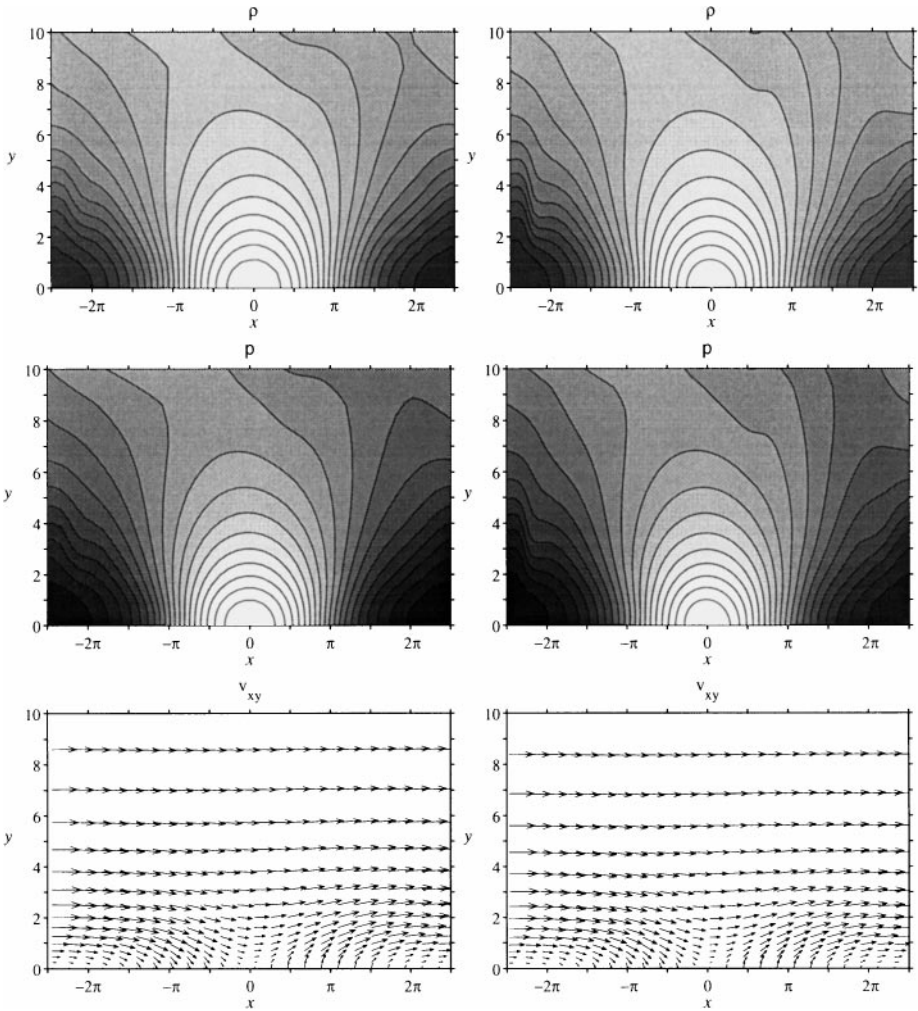
FIG. 8. Kelvin–Helmholtz instability in a periodic system. The left-hand column uses 48×30 points and the right-hand column uses 96×60 points. There are 20 contours for density and pressure and the gray colormap means that the lighter color area has a greater value. The density range is from 0.79 to 1.2, the pressure range is from 0.31 to 0.72, and the maximum value for the velocity is 1.26.

much stronger than that found in the periodic system. The flow components at $t = 120$ and $t = 145$ are shown, respectively, in Figs. 9 and 10. The gross feature in this calculation is similar to that in [31].

In these calculations, the components of B_x, B_y, and v_z are always zero and the evolution of B_z follows closely with that of the density. By defining the pressure to be p^*, these MHD calculations are identical to the Euler calculations. Therefore, the differences between the periodic model and the convective model are also valid in the Euler system. For these calculations, results do not depend on whether the 8×8 eigen-system or the 7×7 eigen-system is used.

Because of its high-order accuracy, the WENO scheme achieves an accuracy comparable with the results of [31], which uses the usual two-step Lax–Wendroff scheme, with many fewer grid points, and with no spurious oscillations. Table V shows a comparison among
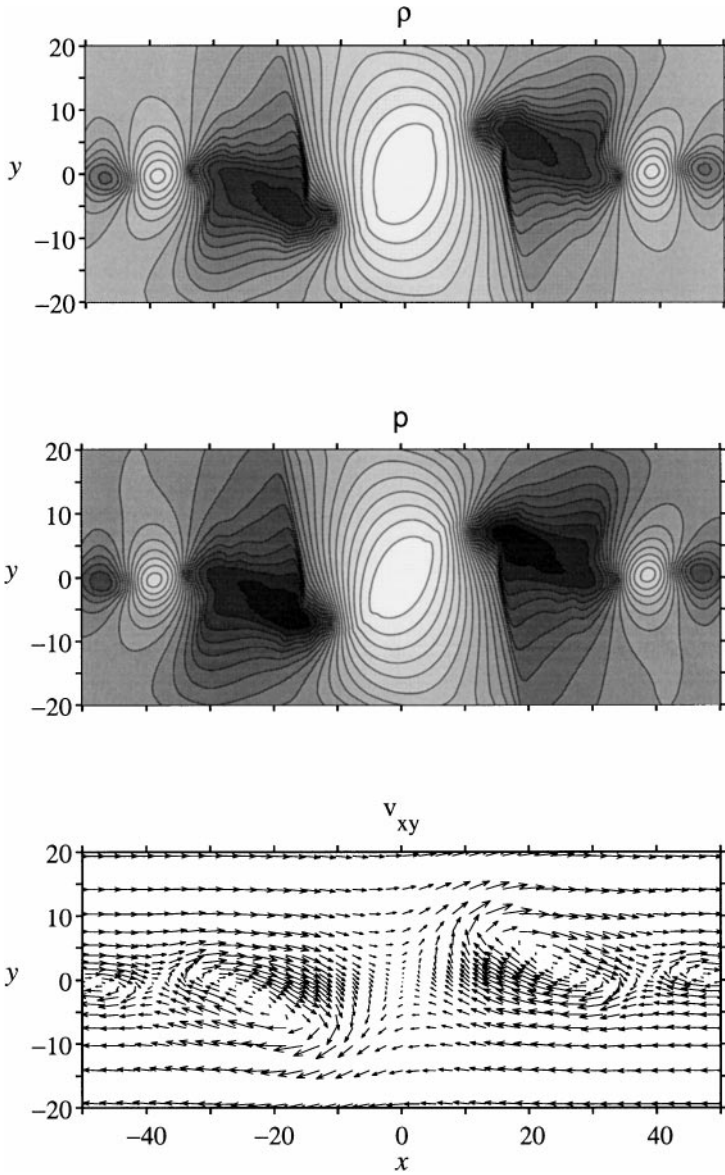
FIG. 9.   The convective Kelvin–Helmholtz instability at $t = 120$. There are 20 contours drawn for density and pressure. The gray scale indicates that the lighter color area has a greater value. The density range is from 0.62 to 1.3, the pressure range is from 0.19 to 0.85, and the maximum value of the velocity is 1.53.

several numerical schemes for the periodic model with a uniform grid in both the x- and y-directions over the computational domain of $[0, 5\pi] \times [-10, 10]$. The first set of calculations is conducted with the 5th-order WENO scheme with various numbers of grid points. A second set (labelled LW1) uses the usual two-step Lax–Wendroff method. For each run, we list the maximum transverse kinetic energy E_T attained and the time when it occurs. For the WENO code, the calculation with the 50×100 grid is already very accurate, reaching about 97% of the saturated kinetic energy. Since the solution is more complicated in the y-direction than in the x-direction, one requires more grid points in the y-direction than in
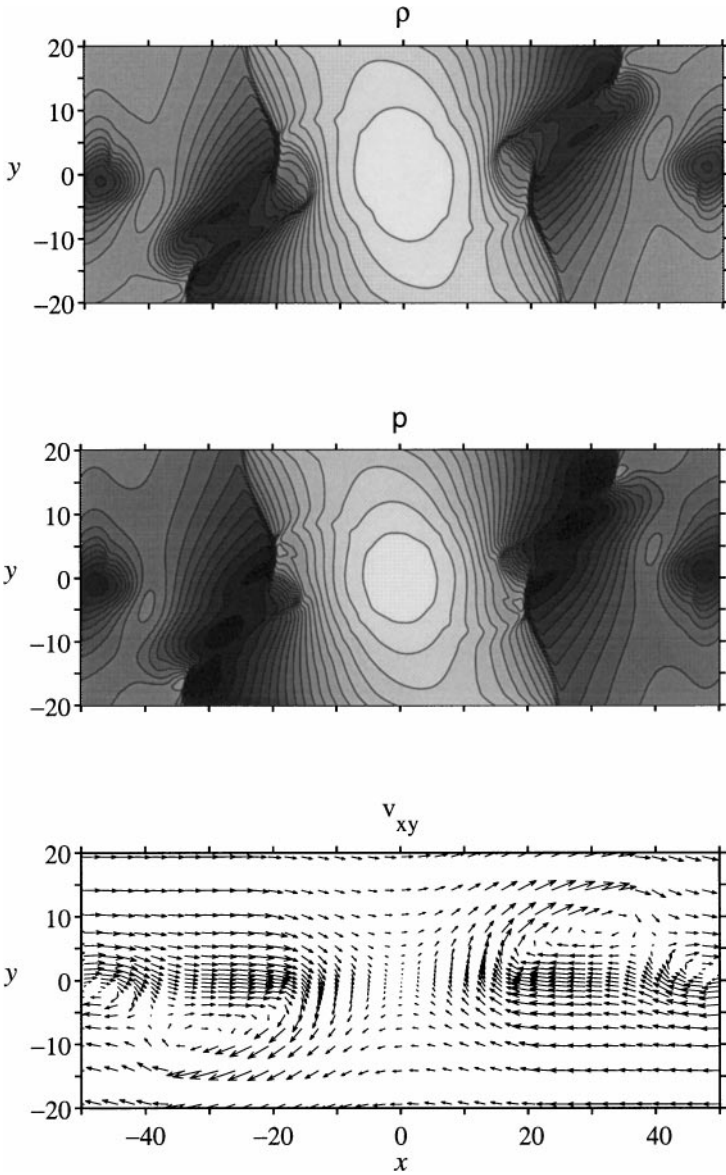
FIG. 10. The convective Kelvin–Helmholtz instability at $t = 145$. There are 20 contours drawn for density and pressure. The gray scale indicates that the lighter color area has a greater value. The density range is from 0.46 to 1.3, the pressure range is from 0.12 to 0.86, and the maximum value of the velocity is 1.89.

the x-direction. The convergence of the solution is demonstrated in Fig. 11, which shows the time evolution of the transverse kinetic energy from the WENO code with 40×80, 50×100, 75×150, and 100×200 grids.

However, the LW1 code does poorly in simulating the Kelvin–Helmholtz instability. With a 50×100 grid, it only reaches about 3% of the converged value. It requires more than 100×600 to attain the 93% level. One main reason is that although the initial configuration is an equilibrium state, it cannot be maintained when dissipation terms, either physical or numerical, are present. Therefore, the Lax–Wendroff scheme, which has larger numerical

TABLE V

Calculations of the Periodic Kelvin–Helmholtz Instability on Various Grids with a 5th-Order WENO Scheme, the Lax–Wendroff Codes for U (LW1) and for $\bar{U}$ (LW2), a 3rd-Order ENO Scheme, and a 2nd-Order Liu–Lax Scheme (LL)

Code	$N_x \times N_y$	E_T	T	$N_x \times N_y$	E_T	T
WENO	30×60	2.283	102.0	40×80	3.365	82.6
	50×100	3.584	80.7	80×100	3.598	80.8
	50×150	3.676	78.4	80×150	3.689	78.4
	75×150	3.689	78.5	100×200	3.703	77.9
LW1	50×100	0.12	79.3	100×200	0.38	80.6
	100×300	2.88	79.1	100×400	3.23	75.8
	150×400	3.23	79.3	100×600	3.43	78.2
LW2	50×100	2.65	77.3	50×200	2.99	78.1
	100×200	3.35	78.5	200×200	3.57	77.5
ENO	40×80	3.014	87.5	50×100	3.342	81.1
	75×150	3.585	79.0	100×200	3.648	78.0
LL	50×100	1.32	78.8	100×200	2.47	64.0
	200×400	3.04	71.8	100×600	3.02	75.5

Note. The saturated (maximum) total transverse kinetic energy (E_T) integrated over $[-5\pi/2, 5\pi/2] \times [-10, 10]$, and the time it occurs (T) are shown for each run.

dissipation terms than the 5th WENO scheme, tends to smooth out more the initial shear-flow profile. As a result, the computed growth of the Kelvin–Helmholtz instability is smaller and the saturated energy level is lower. One can remedy this situation by solving $\bar{U}$ instead of U in terms of $\bar{U}_t = (U - U_0)_t = -(F - F_0)_x - (G - G_0)_y$, where the quantities with subscript 0 refer to the initial conditions. Therefore, $\bar{U}$ is zero if there is no perturbation and the initial U_0 profile is kept. This method was employed in [31]. The third set of the runs
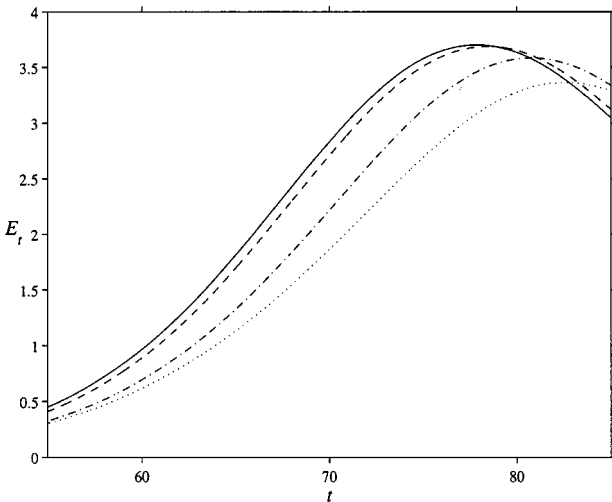

FIG. 11. Time evolution of the total transverse kinetic energy integrated over $[-L/2, L/2] \times [-H, H]$ for periodic Kelvin–Helmholtz instability from $t = 55$ to $t = 85$. The results from 40×80, 50×100, 75×150, and 100×200 grids are plotted as dotted, dashdot, dashed, and solid curves, respectively.

(labelled LW2) in Table V was carried out in this way using the two-step Lax–Wendroff scheme. The result shows that they improve greatly over the second set and with a 200×200 grid, they achieve about the same energy level as the WENO scheme with a 50×100 grid.

The next two sets use a 3rd-order ENO scheme [27] and a 2nd-order Liu–Lax scheme [16]. As expected, for being a 3rd-order accurate rather than a 5th-order accurate as WENO, the ENO scheme requires more grid points than WENO to achieve the same saturation level. The ENO result on a 75×150 grid is about the same as the WENO result on a 50×100 grid. The LL scheme is better than LW1 but is not as accurate as LW2. By fitting E_T with the expression $E_T = E_{T\infty} + a(\Delta x)^n$, with constant $E_{T\infty}$ and a, for the results on 40×80, 50×100, 75×150, and 100×200 grids, we obtain $n \approx 4.6$ and 2.8 for WENO and ENO, respectively. For the WENO scheme, the expression $E_T = 3.707 - 25(\Delta x)^{4.6}$ gives $E_T = 3.368, 3.585, 3.688$, and 3.702, for 40×80, 50×100, 75×150, and 100×200 grids, respectively. These values of E_T agree with those values listed in Table V. Similarly, the expression $E_T = 3.707 - 9.6(\Delta x)^{2.8}$ gives a reasonable fit for the ENO results. We have also compared the total transverse kinetic energy at a fixed time $t = 75$. For the WENO scheme, the values of the transverse kinetic energy are 2.69, 3.12, 3.51, and 3.58 on the respective 40×80, 50×100, 75×150, and 100×200 grids. The order of accuracy is about 4.2. These figures are consistent with the order of accuracy of these schemes and agree with the numerical experiments of Shu and Osher [27] and Jiang and Shu [14].

A higher-order accurate code generally requires more operations than a lower-order accurate code. By counting the number of operations, we can estimate that the computer time per grid-point update is increased by a factor of about 4 from the 2nd-order Liu–Lax scheme to the 5th-order WENO scheme. A factor of 2 comes from the increase of the number of steps in the Runge–Kutta time integration, and a factor of 2 is from the computation of the flux. Similarly, the increase from a 3rd-order ENO to the 5th-order WENO is a factor of about 2. These increases do not depend on the dimensionality. These factors are observed on serial workstations. However, on a vector computer such as the CRAY T90, the 5th-order WENO scheme can be faster than a 3rd-order ENO because fewer IF statements are used in WENO than in ENO [14]. Of course a 2nd-order Lax–Wendroff scheme, which uses no wave decomposition, is faster than WENO by a factor of more than 100.

We note that the comparison in Table V depends on the physical problems. But let us assume that its result can be extended to some 3D problems and one can achieve the same accuracy with 50 grid points in each direction using the 5th-order WENO code, with 75 grid points using the 3rd-order ENO code, and with 150 points using the 2nd-order Liu–Lax code. Then ENO and Liu–Lax codes require 50 and 300%, respectively, more time steps than the WENO code. Therefore, despite the fact that the WENO scheme requires more operations per grid-point update, the WENO scheme is the most efficient among the three. The ENO scheme needs 2.5 times more CPU time than the WENO scheme and the Liu–Lax scheme requires 20 times more than the WENO scheme.

3.4. *Orszag–Tang MHD Turbulence Problem*

In this section, we consider the evolution of a compressible Orszag–Tang vortex system [18]. The problem contains many significant features of MHD turbulence and has been extensively studied by Dahlurg and Picone [6] and Picone and Dahlburg [19]. Because of its

complex evolution, which involves the interactions between several shock waves generated as the vortex system evolves, it has also been used as a test problem for numerical codes by Zachary *et al.* [36] and by de Fainchtein *et al.* [10]. Our initial setup is identical to that of Zachary *et al.* with the initial data

$$\rho(x, y, 0) = \gamma^2, \qquad v_x(x, y, 0) = -\sin y, \qquad v_y(x, y, 0) = \sin x,$$

$$p(x, y, 0) = \gamma, \qquad B_x(x, y, 0) = -\sin y, \qquad B_y(x, y, 0) = \sin 2x,$$

where $\gamma = 5/3$. Thus, initially, the root mean square (rms) values of velocity and the magnetic field are both 1; the initial average Mach number is 1 and the average plasma beta is 10/3. The computational domain is $[0, 2\pi] \times [0, 2\pi]$ with periodic boundary conditions in both the x- and y-directions. As in the calculations of Zachary *et al.*, we used a uniform 192×192 grid.

The calculations were performed with both the 7×7 eigen-system and the 8×8 eigen-system, each with or without the correction step for enforcing the divergence-free condition for the magnetic field. The Poisson equation for the potential ϕ is again solved using a relaxation method. Without the correction procedure, the calculations with either the 7×7 system or the 8×8 system become numerically unstable when the pressure turns to negative. It occurs at $t \sim 3.9$ using the 8×8 eigen-system and at $t \sim 2.5$ using the 7×7 eigen-system. A plausible explanation for the difference is that the 7×7 system has no diffusion terms for the flux corresponding to the B_x (B_y) component in the x (y) direction. By adding some diffusion to the corresponding equations, such as a 4th-order diffusion to the evolution equation for B_x and a similar term for the evolution equation of B_y, we can bring the code with the 7×7 eigen-system up to the level of the 8×8 system. However, these additional diffusion terms are not needed when the correction procedure for enhancing the $\nabla \cdot \mathbf{B} = 0$ condition is employed.

With the addition of the correction procedure, both 7×7 and 8×8 systems are numerical stable and give almost the same results. We have successfully run both up to $t = 8$. This is another demonstration that the divergence-free condition for the magnetic field plays an important role in the MHD calculations. The results using WENO with the 8×8 eigen-system are shown in Figs. 12, 13, and 14 for $t = 0.5$, 2, and 3, respectively. Tables VI and VII show the errors of the code at $t = 0.2$ and 0.5, respectively. The errors are defined as the deviations of the density from its value obtained on a 512×512 grid. For both cases high order of accuracy is achieved starting with a 64×64 grid. For the case at $t = 0.5$, the errors are larger because of the high gradients in the solution (Fig. 12).

TABLE VI
Accuracy on the Orszag–Tang Vortex Problem at $t = 0.2$ Using the 5th-Order WENO Scheme with $N \times N$ Grid Points

N	L_1 error	L_1 order	L_∞ error	L_∞ order
16	1.8e-2	—	6.6e-2	—
32	3.5e-3	2.4	1.2e-2	2.5
64	2.8e-4	3.6	1.3e-3	3.2
128	1.4e-5	4.3	2.2e-4	2.6
256	6.8e-7	4.4	5.9e-6	5.2

TABLE VII
Accuracy on the Orszag–Tang Vortex Problem at $t = 0.5$ Using the 5th-Order WENO Scheme with $N \times N$ Grid Points

N	L_1 error	L_1 order	L_1^* error	L_1^* order	L_∞ error	L_∞ order
16	7.9e-2	—	2.6e-2	—	1.2	—
32	1.3e-2	2.6	8.3e-3	1.6	3.4e-1	1.8
64	1.2e-3	3.4	6.1e-4	3.8	2.6e-2	3.7
128	1.4e-4	3.1	3.4e-5	4.2	5.0e-3	2.4
256	2.3e-5	2.6	4.4e-6	3.0	4.9e-4	3.4

Note. L_1 and L_∞ cover the whole computational domain while L_1^* covers only the region within $0.9\pi \leq x \leq 1.1\pi$ and $0.9\pi \leq y \leq 1.1\pi$.
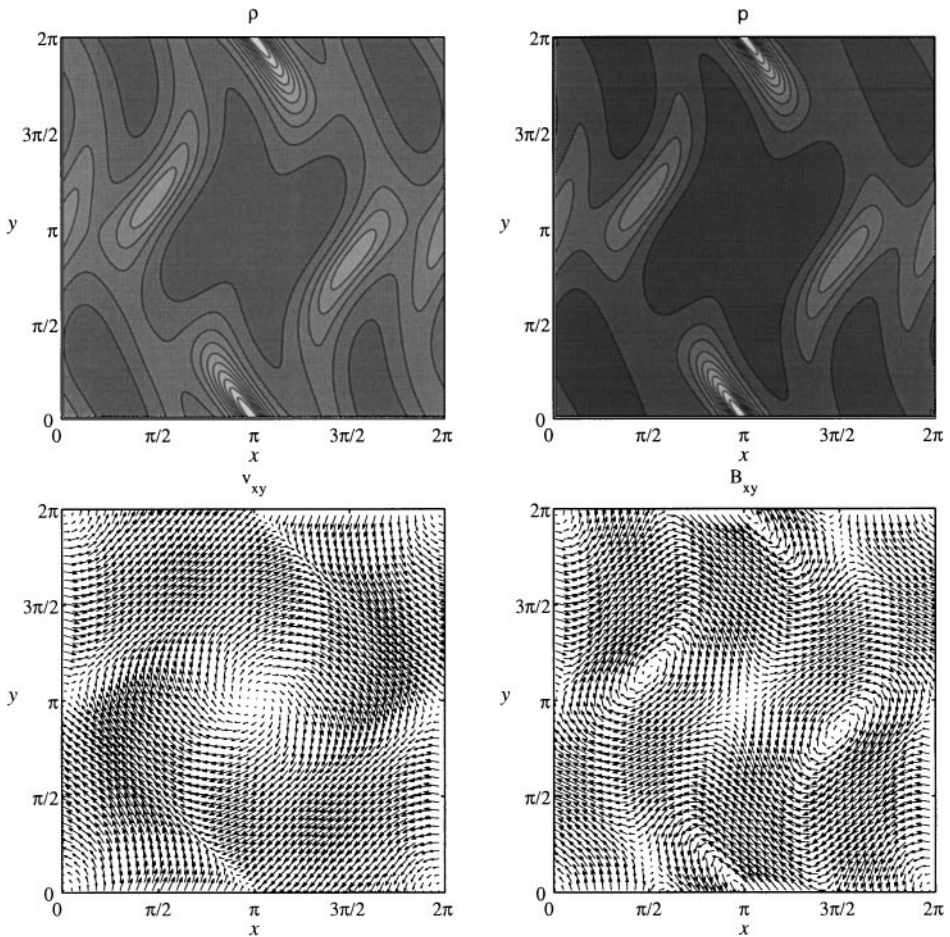
FIG. 12. The Orszag–Tang MHD turbulence problem with a uniform 192×192 grid at $t = 0.5$. The 8×8 eigen-system is used. There are 12 contours for both density and pressure. The gray scale means that the brighter color area has a larger value. The range for ρ is from 2.1 to 5.8 and it is from 1.0 to 5.8 for p. The maximum values of $|v|$ and $|B|$ are 1.6 and 1.6, respectively.
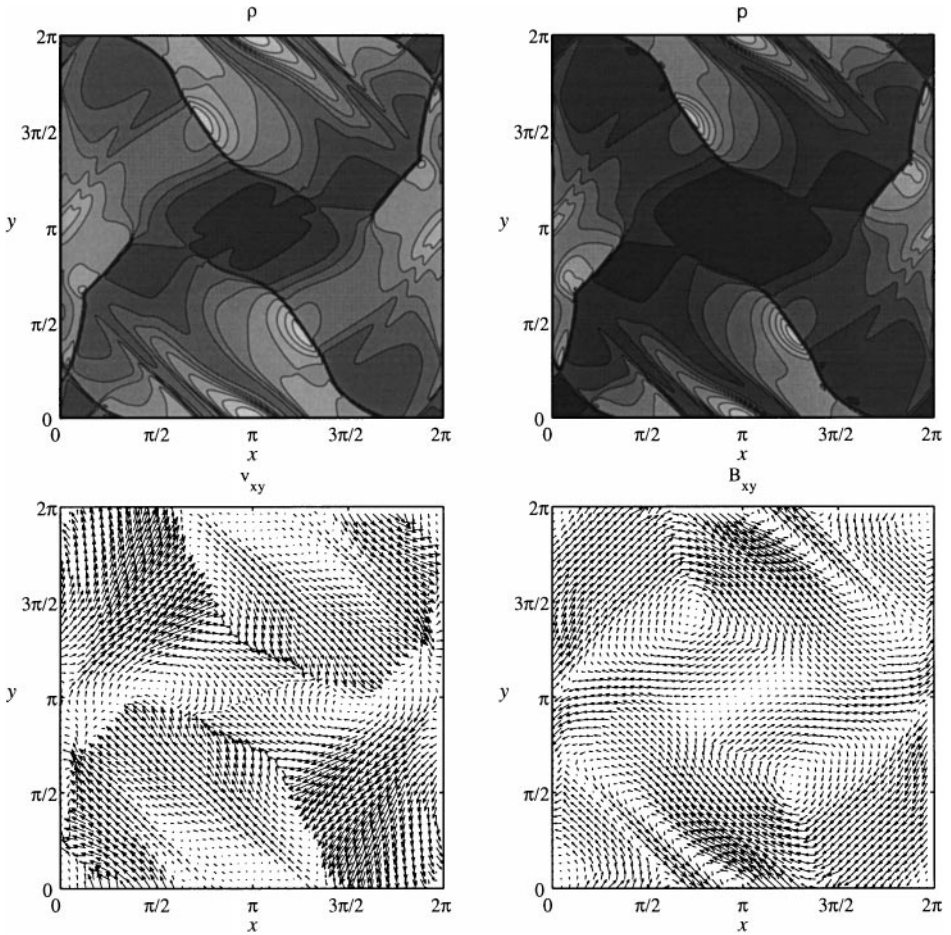
FIG. 13. The Orszag–Tang MHD turbulence problem with a uniform 192×192 grid at $t = 2$. The 8×8 eigen-system is used. There are 12 contours for both density and pressure. The gray scale means that the brighter color area has a larger value. The range for ρ is from 0.64 to 6.2 and it is from 0.14 to 6.9 for p. The maximum values of $|v|$ and $|B|$ are 1.6 and 2.8, respectively.

The results at $t = 3$ agree with the one given by Zachary *et al.* [36]. It is seen that the evolution of the system is very complex and many shocks of all kinds are formed. For instance, in Fig. 13, an intermediate shock is formed at the shock front from (x, y) $\sim (3\pi/2, 0)$ to $(\pi, 3\pi/4)$. Across this shock wave, the transverse component of the magnetic field changes its sign, which is a property of an intermediate shock. On the other hand, for fast and slow shocks, the transverse component does not change sign and its magnitude increases from upstream to downstream for fast shocks and decreases for slow shocks. In Fig. 14, the shock front from $(x, y) \sim (3\pi/2, \pi/2)$ to $(5\pi/4, 3\pi/4)$ is a fast shock and the front from $(x, y) \sim (\pi, 3\pi/4)$ to $(\pi/2, \pi)$ is a slow shock.

Figure 15 plots the pressure distributions along a cut at $y = 0.625\pi$ for the results at $t = 3$. Shown are results from three calculations: one with the 8×8 system without the correction step, one with the 8×8 system with the correction procedure, and one with the 7×7 system with the correction step. The two that include the correction procedure provide similar results. It tends to be more oscillatory when the $\nabla \cdot \mathbf{B} = 0$ condition is not enforced; although all three results are consistent with each other at this time.
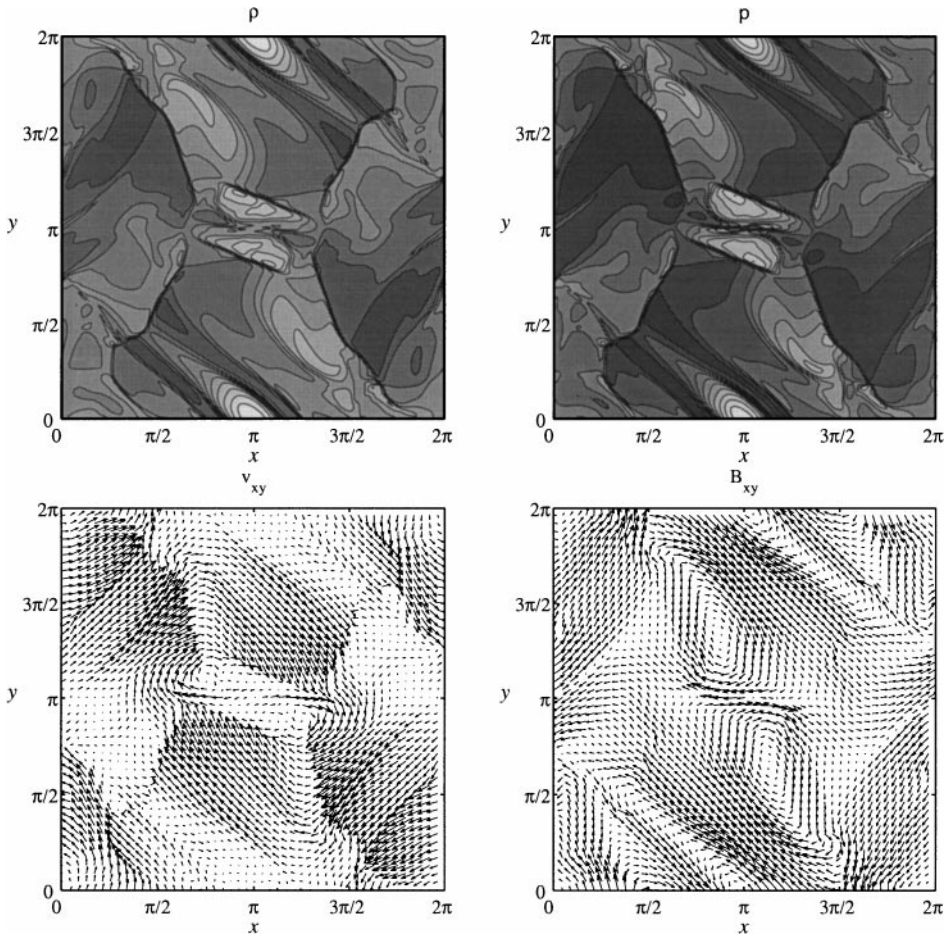
FIG. 14. The Orszag–Tang MHD turbulence problem with a uniform 192×192 grid at $t = 3$. The 8×8 eigen-system is used. There are 12 contours for both density and pressure. The gray scale means that the brighter color area has a larger value. The range for ρ is from 1.1 to 6.2 and it is from 0.36 to 6.3 for p. The maximum values of $|v|$ and $|B|$ are 1.7 and 3.0, respectively.

4. CONCLUSIONS

In this paper we have presented a 5th-order WENO finite difference scheme for ideal MHD. Its application from hydrodynamic problems to MHD is straightforward, although the MHD code requires considerably more work than the Euler code because of the complexity associated with the MHD eigen-system. As in the Euler code, characteristic wave decomposition and flux splitting are used in the MHD code. The same WENO approximation for the fluxes at the interfaces is also employed. Also, the extension to multi-spatial dimensions is carried out by calculating the flux dimension-by-dimension. For both Euler and MHD codes, there is a restriction on the grid. The finite difference ENO/WENO scheme of third- or higher-order accuracy can only apply to a uniform grid or a smoothly varying grid.

The numerical tests show that the new MHD codes are robust and capture shocks and rarefaction waves well. The tests also indicate the importance of enforcing the divergence free condition for the magnetic field. It helps to maintain the numerical stability.
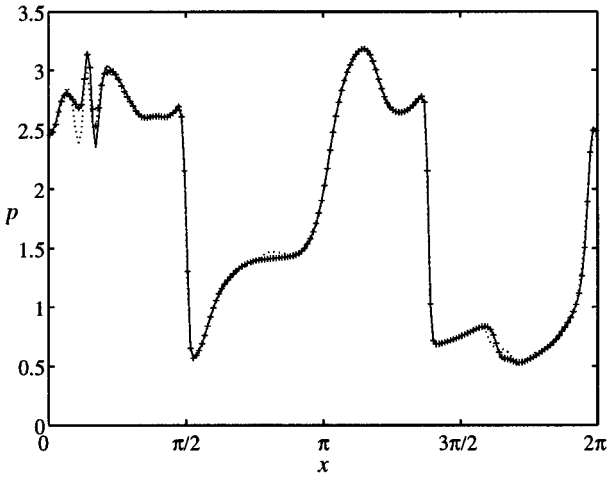
FIG. 15. The pressure distributions along a cut at $y = 0.625\pi$ for the results of the Orszag–Tang MHD turbulence problem at $t = 3$. Shown are results from three calculations: one with the 8×8 system without the correction step (dotted curve), one with the 8×8 system and with the correction procedure (marked with $+$), and one with the 7×7 system and with the correction step (solid curve).

There is a clear advantage of using the higher-order scheme. In a 2D test problem for the Kelvin–Helmholtz instability, the 5th-order WENO code can attain same accuracy as the 2nd-order schemes with fewer grid points, which is an important consideration for three-dimensional simulations. Although the 5th-order WENO scheme requires more operations per grid-point update, it may actually use much less CPU time than a 2nd-order upwind code with wave decomposition in the overall calculation. The main benefit, however, is the feasibility of running a very large large-scale simulation with the 5th-order WENO scheme. For instance, it is possible to run a 500^3 system with the WENO scheme on a currently available large computer system, but it will require additional computational work to run a 1500^3 system with the 2nd-order scheme.

Because of its small numerical dissipation, the high-order accurate WENO code may be very useful in simulating physical problems where small physical dissipation is required. For example, it may be useful in the 3D MHD model of the Earth's magnetosphere; see, e.g., [30]. The interaction of the solar wind with the geomagnetic field results in the formation of a bow shock and a magnetopause. The magnetopause is an interface between the magnetosheath and the magnetosphere. Since there are both magnetic shear and flow shear across this boundary, the magnetic reconnection process and Kelvin–Helmholtz instability may operate there. However, because of large numerical diffusion terms, reconnection processes overwhelm the magnetospheric dynamics in most current global models. Using a higher-order scheme may help to reduce the dissipation terms and thus help to realize the Kelvin–Helmholtz instability in a 3D model.

In sum, we believe that there are uses of higher-order schemes. But we certainly do not exclude any 2nd-order or 1st-order schemes, which can be quite efficient in 1D calculations, or any adaptive codes, which are not included in our comparison. We should also note that the efficiency comparison definitely depends on the physical problems. Lower-order codes may be more efficient than higher-order codes in some problems. In addition, to achieve a high-order accuracy, high-order accurate boundary conditions are required. This may require more work for some calculations.

As mentioned in the Introduction, when the rotation of the magnetic field exists, the evolution of the MHD system may depend on the dissipation mechanism, which according to the Navier–Stokes MHD equations, includes bulk and shear viscosities, resistivity, and heat conductivity. Since no explicit diffusion terms are included in the code, the solution may thus depend on numerical dissipation. The situation may be corrected in our future code improvement by using the WENO shock capturing scheme for the fast and slow shock, and by resolving the shock structure for the intermediate shock.

ACKNOWLEDGMENTS

REFERENCES

1. N. Aslan, Numerical solutions of one-dimensional MHD equations by a fluctuation approach, *Int. J. Numer. Methods Fluids* **22**, 569 (1996).

2. J. U. Brackbill and D. C. Barnes, The effect of nonzero div B on the numerical solution of the magnetohydrodynamic equations, *J. Comput. Phys.* **35**, 426 (1980).

3. M. Brio and C. C. Wu, Characteristic fields for the equations of magnetohydrodynamics, in *Nonstrictly Hyperbolic Conservation Laws*, edited by B. Keyfitz and H. C. Kranzer (Am. Math. Soc., Providence, RI, 1987), p. 19.

4. M. Brio and C. C. Wu, An upwind differencing scheme for the equations of ideal magnetohydrodynamics, *J. Comput. Phys.* **75**, 400 (1988).

5. D. A. Clarke, M. L. Norman, and J. O. Burn, Numerical simulations of a magnetically confined jet, *Ap. J.* **311**, L63 (1986).

6. R. B. Dahlburg and J. M. Picone, Evolution of the Orszag–Tang vortex system in a compressible medium. I. Initial average subsonic flow, *Phys. Fluids B* **1**, 2153 (1989).

7. W. Dai and P. R. Woodward, A high-order Godunov-type scheme for shock interactions in ideal magnetohydrodynamics, *SIAM J. Sci. Comput.* **18**, 957 (1997).

8. W. Dai and P. R. Woodward, A simple finite difference scheme for multidimensional magnetohydrodynamical equations, *J. Comput. Phys.* **142**, 331 (1998).

9. C. R. Evans and J. F. Hawley, Simulation of magnetohydrodynamic flows: A constrained transport method, *Ap. J.* **332**, 659 (1988).

10. R. de Fainchtein, S. T. Zalesak, R. Löhner, and D. S. Spicer, Finite element simulation of a turbulent MHD system: Comparison to a pseudo-spectral simulation, *Comput. Phys. Comm.* **86**, 25 (1995).

11. A. Harten, High resolution schemes for hyperbolic conservation laws, *J. Comput. Phys.* **49**, 357 (1983).

12. A. Harten, B. Engquist, S. Osher, and S. Chakravarthy, Uniformly high-order accurate essentially non-oscillatory schemes, III, *J. Comput. Phys.* **71**, 231 (1987).

13. A. Jeffrey and T. Taniuti, *Non-linear Wave Propagation*, (Academic Press, New York, 1964).

14. G.-S. Jiang and C.-W. Shu, Efficient implementation of weighted ENO schemes, *J. Comput. Phys.* **126**, 202 (1996).

15. C. F. Kennel, R. D. Blandford, and C. C. Wu, Structure and evolution of small-amplitude intermediate shock waves, *Phys. Fluids B* **2**, 253, (1990).

16. X.-D. Liu and P. D. Lax, Positive schemes for solving multi-dimensional hyperbolic systems of conservation laws, *J. Comput. Fluid Dynam.* **5**, 133 (1996).

17. X.-D. Liu, S. Osher, and T. Chan, Weighted essentially non-oscillatory schemes, *J. Comput. Phys.* **115**, 200 (1994).

18. S. A. Orszag and C. M. Tang, Small-scale structure of two-dimensional magnetohydrodynamic turbulence, *J. Fluid. Mech.* **90**, 129 (1979).

19. J. M. Picone and R. B. Dahlburg, Evolution of the Orszag-Tang vortex system in a compressible medium. II. Supersonic flow, *Phys. Fluids B* **3**, 29 (1991).

20. K. G. Powell, P. L. Roe, R. S. Myong, T. Gombosi, and D. de Zeeuw, An upwind scheme for magnetohydrodynamics, in *AIAA 12th Computational Fluid Dynamics Conference, San Diego, CA, June 19–22, 1995*, p. 661.

21. P. L. Roe, Approximate Riemann solvers, parameter vectors, and difference schemes, *J. Comput. Phys.* **43**, 357 (1981).

22. P. L. Roe and D. S. Balsara, Notes on the eigensystem of magnetohydrodynamics, *SIAM J. Appl. Math.* **56**, 57 (1986).

23. D. Ryu and T. W. Jones, Numerical magnetohydrodynamics in astrophysics: Algorithm and tests for one-dimensional flow, *Ap. J.* **442**, 228 (1995).

24. D. Ryu, T. W. Jones, and A. Frank, Numerical magnetohydrodynamics in astrophysics: Algorithm and tests for multidimensional flow, *Ap. J.* **452**, 785 (1995).

25. C.-W. Shu, Total-variation-diminishing time discretizations, *SIAM J. Sci. Stat. Comput.* **9**, 1073 (1988).

26. C.-W. Shu, *Essentially Non-oscillatory and Weighted Essentially Non-oscillatory Schemes for Hyperbolic Conservation Laws*, ICASE Report 97-65, 1997.

27. C.-W. Shu and S. Osher, Efficient implementation of essentially non-oscillatory shock-capturing schemes, II, *J. Comput. Phys.* **83**, 32 (1989).

28. G. A. Sod, A survey of several finite difference methods for systems of nonlinear hyperbolic conservation laws, *J. Comput. Phys.* **27**, 1 (1978).

29. T. Tanaka, Generation mechanisms for magnetosphere-ionosphere current systems deduced from a three-dimensional MHD simulation of the solar wind-magnetosphere-ionosphere coupling processes, *J. Geophys. Res.* **100**, 12,057 (1995).

30. C. C. Wu, Global MHD Model of the Earth's magnetosphere, in *Solar Terrestrial Physics, Principles and Theoretical Foundations*, edited by R. L. Carovillano and J. M. Forbes (Reidel, Dordrecht, l983), p. 369.

31. C. C. Wu, Kelvin–Helmholtz instability at the magnetopause boundary, *J. Geophys. Res.* **91**, 3042 (1986).

32. C. C. Wu, On MHD intermediate shocks, *Geophys. Res. Lett.* **14**, 668 (1987).

33. C. C. Wu, Formation, structure, and stability of MHD intermediate shocks, *J. Geophys. Res.* **95**, 8149 (1990).

34. C. C. Wu, Magnetohydrodynamic Riemann problem and the structure of the magnetic reconnection layer, *J. Geophys. Res.* **100**, 5579 (1995).

35. S. Xu, T. Aslam, and D. Stewart, High resolution numerical simulation of ideal and non-ideal compressible reacting flows with embedded internal boundaries, *Combustion Theory Model.* **1**, 113 (1997).

36. A. L. Zachary, A. Malagoli, and P. Colella, A higher-order Godunov method for multi-dimensional ideal magnetohydrodynamics, *SIAM J. Sci. Comput.* **15**, 263 (1994).